

# Combining molecular simulation and experiment to understand the effect of moisture on methane adsorption in kerogens

Wei Li<sup>a,\*</sup>, Lee A. Stevens<sup>a,\*</sup>, Bo Zhang<sup>b</sup>, Dingye Zheng<sup>c,d</sup>, Colin E. Snape<sup>a</sup>

<sup>a</sup> University of Nottingham, Low Carbon Energy and Resources Technologies Group, Faculty of Engineering, Energy Technologies Building, Triumph Road, Nottingham NG7 2TU, UK

<sup>b</sup> Schlumberger Technologies (Beijing) Ltd, Beijing 100000, China

<sup>c</sup> Sinopec Petroleum Exploration and Production Research Institute, Beijing 100083, China

<sup>d</sup> State Key Laboratory of Petroleum Resources and Prospecting, China University of Petroleum, Beijing 102249, China

## ARTICLE INFO

### Keywords:

Kerogen  
Moisture  
Molecular simulation  
Microporosity  
Sorption sites

## ABSTRACT

There is a limited understanding of the critical impact moisture has on shale gas resource estimation by affecting gas adsorption and pore structure. Laboratory experiments on dry and 95% relative humidity (R.H.) isolated kerogens are combined with Grand Canonical Monte Carlo (GCMC) and Molecular Dynamic (MD) simulations for kerogen models, including matrix and slits (0.5, 1.0, 1.5, and 2.0 nm) with a range of moisture contents (0–42 wt % on a total organic carbon content (TOC) basis) to better understand how moisture impacts methane adsorption. Higher methane adsorption capacities ( $Q_m$ ) and micropore volumes ( $V_{micro}$ ) are observed for simulated kerogens since all pores in GCMC are accessible. Moisture has a negative effect on  $Q_m$ , displaying 'rapid', 'gentle', and 'slow' stages with increasing moisture in simulation. Reductions in  $Q_m$  (61–75%) and  $V_{micro}$  (88–93%) are obtained for isolated kerogens containing moisture of 38–70 wt% TOC with up to 56% of the moisture in micropores. The same  $Q_m$  and  $V_{micro}$  reductions can be reached for the simulated kerogens with moisture contents of 4–24 wt% TOC for matrix and slits. The relative coordination number ( $C_r$ ) from MD simulation indicates water has a stronger affinity than methane for all functional groups with preferred sorption sites like carboxyl (COOH) under reservoir conditions. The microporosity controls condensed water cluster size. Water adsorbed in ultra-micropores (<0.7 nm) leads to 'rapid' reduction, the 'gentle'  $Q_m$  reduction stage arises from water condensing, and filling of remaining pores at the highest moisture is related to the 'slow'  $Q_m$  reduction stage. Therefore, water reduces the methane adsorption capacity of kerogen mainly by occupying and blocking the pore volume rather than competing directly with methane for sorption sites.

## 1. Introduction

Gas in place (GIP) for shales is usually estimated from the sum of adsorbed and free gas, and considering the moisture impact under reservoir conditions provides a more accurate result [1–4]. As the primary insoluble organic matter in shale, kerogen plays a crucial role in shale gas evaluation and production [4–7]. >50% of adsorbed gas in shale is contributed by isolated kerogens at dry [4,6,8], and 95% relative humidity (R.H.) moisture-equilibrated (wet) conditions [4], due to the well-developed microporosity. The generally larger porosity in higher maturity kerogen arises from the generation and release of hydrocarbons [9–13].

Laboratory results indicate moisture has a negative impact on

methane adsorption capacity, which, together with occupying some pore volumes, results in GIP being over-estimated [4,5,14–16]. Reductions of 20–85% in methane adsorption capacities at 97% relative humidity (R.H.) for moisture-equilibrated shales have been reported [5,15,17,18]. It was believed that this is mainly due to moisture blocking the available adsorption sites/pores for methane in clay directly and in organic matter indirectly [19,20], since hydrophilic clay minerals are the main component to adsorb water in shale [21–24].

Whereas, recent experiments reveal that the amount of water absorbed in shale is positively related to the content of organic matter, possibly because of its oxygen-containing functional groups and, compared to the mineral matrix, larger specific surface area [18,25,26], confirming water can affect methane adsorption in the organic matter

\* Corresponding author.

E-mail address: [Lee.Stevens@nottingham.ac.uk](mailto:Lee.Stevens@nottingham.ac.uk) (L.A. Stevens).

<https://doi.org/10.1016/j.cej.2022.139942>

Received 20 August 2022; Received in revised form 15 October 2022; Accepted 17 October 2022

Available online 2 November 2022

1385-8947/© 2022 The Author(s). Published by Elsevier B.V. This is an open access article under the CC BY license (<http://creativecommons.org/licenses/by/4.0/>).

directly. The negative effects of moisture on methane adsorption capacity of isolated kerogens have been revealed by high-pressure methane adsorption experiments [4], where >50% of the methane adsorption capacities are lost for 95%R.H. moisture-equilibrated (wet) samples.

Molecular simulation as a practical theory approach, including molecular dynamic (MD) and Grand Canonical Monte Carlo (GCMC) simulation, is widely applied to investigate gas/oil adsorption for kerogen in shale [27–31]. GCMC is an effective method to study the gas adsorption capacity by the statistic probabilities analysis method, and MD simulation can reveal the dynamic adsorption behaviour by analysing the physical movements of atoms and molecules [32–34]. Although kerogen is composed of heterogeneous amorphous polymers covering a wide range of compositions it can be classified into four types (I, II, III, and IV) and different maturities, with the same type and maturity kerogen sharing a similar elemental composition, functional groups and structural features [6,7,12,35,36]. The composition and structural parameters of different kerogens measured by the X-ray and Solid-State  $^{13}\text{C}$  nuclear magnetic resonance (NMR) [37] are used for constructing the representative realistic 3D kerogen molecules [38], which are widely applied in simulation research on kerogen [30,39–41]. Kerogen has complex pore network where different pore shapes could exist [42]. Different kerogen models including graphene proxies [43,44], matrices or matrices with dummy pores [29,45,46], kerogen slits [27,40,47–49], and kerogen cylindrical pore models [42,50,51] have been constructed in simulation, providing insight into kerogen pore structure and networks. Although the methane adsorption amounts from slit kerogens are slightly higher than that from cylindrical kerogen models, their adsorption isotherms present a similar trend [42,50]. These simulated kerogen models cover the ultra-micropores (<0.7 nm), super-micropores (0.7–2.0 nm), and some mesopores up to 10 nm.

In contrast to the limited laboratory research on wet isolated kerogens [4], the negative effects of moisture on methane adsorption capacity of simulated kerogen have been revealed by GCMC and MD simulations [30,52–54]. Significantly decreased methane adsorption was observed for the moist kerogen matrix models with moisture content from 0.6 to 2.4 wt% [30,54,55], and from 0.6 to 3.0 wt% [56]. Molecular simulations have also been carried out on kerogen matrix under a wider range of moisture contents from 0.5 to 6.0 wt% to illustrate the moisture and salinity effects on methane adsorption, and the results indicate 42.5% methane adsorption capacity is reduced for gas window kerogen with the moisture content of 6.0 wt% at 65 °C [52].

The reduced methane adsorption capacity in wet kerogen matrices could result from the limited pore volume and/or water could compete with the sorption sites for methane [45,54,55], as water has a higher affinity with kerogen than methane [46]. However, much more detailed research on how water affects methane adsorption in kerogen, considering the difference of physical micropore structure and exact chemical components, is still needed. Moreover, the limited moisture content up to 3 wt% for kerogen in most simulations which was taken from studies on coal [57,58] or shales [59], is much less than the moisture content in isolated kerogen from the experiment (about 15 wt% at 95%R.H.) [4]. The molecular simulation work to date has only involved making simple comparisons of the predicted methane adsorption isotherms to experimental data for coals, shales, and dry isolated kerogens [45,54,55] due to the very limited experimental data on wet kerogens. In addition, the models containing moisture used in simulations to date are mainly on the kerogen matrix, covering pores <1 nm. However, the larger micropores (1–2 nm) are essential for methane adsorption [60], and moisture can block the pore or/and pore neck <1.3 nm and impact the pore connectivity of kerogens [4].

This study is the first to present a detailed comparison of the impact of moisture on methane adsorption in kerogen combining experimental data and molecular simulation. The mechanistic description of the effects, considering the microporosity, functional groups and their combined effect is also revealed. Dry and moist kerogen models (matrix, 0.5,

1.0, 1.5, and 2.0 nm slits) covering the ultra (<0.7 nm) and super-micropores (0.7–2.0 nm) are constructed for the molecular dynamic (MD) and the Grand Canonical Monte Carlo (GCMC) simulation. The consistency of moisture content, microporosity, and methane adsorption capacity between experiment and simulation results are compared, which can provide solid foundations for further simulation on moist kerogen. Moreover, the findings in this study can provide a new perspective on understanding methane adsorption in wet kerogen to better estimate gas in place for shales.

## 2. Methodology

### 2.1. Samples and laboratory experiments

Experimental data of three isolated gas-window kerogen concentrates (K1, K2, GHK3) have been obtained from two China shales and one UK shale by demineralisation [4]. The two China shales are from Wufeng-longmaxi Formation, Sichuan Basin, with Type II kerogen [14,61]. The Grange Hill UK shale is from Bowland Basin mixed with Type II, III, and IV kerogens, with Type II kerogen predominated [62,63]. Both dry and wet (95%R.H. moisture equilibrated) isolated kerogens were prepared. The pore characteristics and methane adsorption capacity of these isolated kerogens were obtained by low-pressure gas ( $\text{CO}_2$ ,  $\text{N}_2$ ) sorption at 0 and  $-196^\circ\text{C}$ , and high-pressure methane adsorption at  $25^\circ\text{C}$  carried out in laboratory conditions by Micromeritics Surface Area and Porosity Analyser (ASAP 2420) and the High-Pressure Volumetric Analyzer (HPVA-100). Non-Local Density Functional Theory (NLDFT) method based on the carbon slit pore model is applied to calculate the pore size distribution (PSD) in this study. Total organic carbon content (TOC) and Vitrinite Reflectance (VR, %Ro) were measured by Leco CHN628 instruments and LEICA DM4500P microscope. The skeleton and bulk densities of kerogens were obtained from Helium pycnometry and Mercury intrusion porosimetry (MIP), with Scanning Electron Microscope (SEM) and Transmission Electron Spectroscopy (TEM) providing the images of kerogens. All these measurements are described in our previous publications [4,14], except TEM, and the preparation of moisture equilibrated kerogens with other different R.H. (10, 30, 50, and 70% R.H.). The flowchart of sample preparation, experiments, and simulations is given in the [Supplementary Information, Figure S1](#), with the details of gas sorption methods presented in Section S1.

#### 2.1.1. Moisture equilibrated sample preparation

Kerogens were dried at  $120^\circ\text{C}$  in a vacuum oven (<0.5 mbar) for 48 h first, before being placed in a vacuum desiccator containing the specific saturated salt solution at a controlled temperature of  $20^\circ\text{C}$  for 48 h. A logger in the desiccator was used to monitor the relative humidity (R.H.) and temperature. The  $95 \pm 2\%$  R.H. moisture equilibrated (wet) samples were prepared by saturated potassium nitrate ( $\text{KNO}_3$ ) solution (8 g  $\text{KNO}_3/10\text{ mL H}_2\text{O}$ ), which are the wet isolated kerogens used for the high-pressure methane adsorption and low-pressure gas adsorption experiments. The 10, 30, 50, and 70% R.H. moisture equilibrated kerogens were prepared with saturated potassium hydroxide (KOH) solution (14 g  $\text{KOH}/10\text{ mL H}_2\text{O}$ ), magnesium chloride ( $\text{MgCl}_2$ ) solution (5 g  $\text{MgCl}_2/10\text{ mL H}_2\text{O}$ ), magnesium nitrate hexahydrate ( $\text{Mg}(\text{NO}_3)_2$ ) solution (18.7 g  $\text{Mg}(\text{NO}_3)_2/10\text{ mL H}_2\text{O}$ ), and potassium iodide (KI) solution (15 g  $\text{KI}/10\text{ mL H}_2\text{O}$ ) [22,64]. The moisture content of kerogens at each condition was calculated from the mass difference.

#### 2.1.2. Transmission Electron Spectroscopy (TEM)

The holey carbon film (EM Resolutions Ltd) was used to support the dry-deposited kerogen powder (particle size < 300 nm). Then a JEOL 2100F Field emission electron gun (FEG) TEM equipped with a Gatan Orius camera is used to analyse kerogen samples, operating at 200 kV. The TEM images of kerogen are obtained by Gatan Digital Micrograph software.

## 2.2. Simulation procedure

Molecular simulations are carried out by BIOVIA Materials Studio software through the all-atom COMPASS force field [65]. It is a widely used high-quality force field to consolidate parameters of organic materials in kerogen research [30,55,66]. Force fields typically include bonded and non-bonded interactions (Figure S2). The covalent bond energy is presented as Equation (1), including the bond angle bending, bond stretching, dihedral angle torsion, and inversion energy. The non-bond covalent energy includes van der Waals energy ( $E_{\text{van}}$ ), Coulomb energy ( $E_{\text{coulomb}}$ ) and hydrogen bond energy ( $E_H$ ) (Equation (2)). In COMPASS force field, van der Waals (vdW) force is expressed by LJ-9-6 function (Equation (3)), the electrostatic force is calculated by the Coulombic equation (Equation (4)), and hydrogen bond impact is considered in the above forces. The atom-based and Ewald summation methods are used for vdW and electrostatic, respectively [33,67], with a cut-off distance of 1.55 nm applied, indicating the interactions beyond this distance are not considered. In addition, the temperature and the pressure in the simulation system are controlled by the Nosé–Hoover thermostat and barostat, respectively [68–71]. It is worth noting that the dissolved methane in water, as well as the swelling of kerogen, is not considered in this simulation study due to their limited effect [72,73].

$$E_{\text{bond}} = E_{\text{bond stretching}} + E_{\text{angle}} + E_{\text{torsion}} + E_{\text{inversion}} \quad (1)$$

$$E_{\text{nonbond}} = E_{\text{van}} + E_{\text{coulomb}} + E_H \quad (2)$$

$$E_{\text{van}} = D_0 \left[ 2 \cdot \left( \frac{R_0}{R_{ij}} \right)^9 - 3 \cdot \left( \frac{R_0}{R_{ij}} \right)^6 \right] \quad (3)$$

$$E_{\text{coulomb}} = \sum_{ij} q_i q_j / R_{ij} \quad (4)$$

where,  $E_{\text{bond}}$  is the bond force,  $E_{\text{angle}}$  is the bond angle bending energy,  $E_{\text{bond stretching}}$  is bond stretching energy,  $E_{\text{torsion}}$  is the dihedral angle torsion energy,  $E_{\text{inversion}}$  is inversion energy, also called out-of-plane interactions terms, which are part of nearly all force-fields for covalent systems energy,  $E_{\text{nonbond}}$  is the non-bond energy,  $E_{\text{van}}$  is the van der Waals force,  $E_{\text{coulomb}}$  is the Coulomb force,  $E_H$  is the hydrogen bond energy,  $R_{ij}$  is the distance between the atoms  $i$  and  $j$ ,  $D_0$  is the equilibrium L-J well depth,  $R_0$  is the equilibrium distance,  $q_i$ ,  $q_j$  are the charges of the atoms ( $i$  and  $j$ ) in the system.

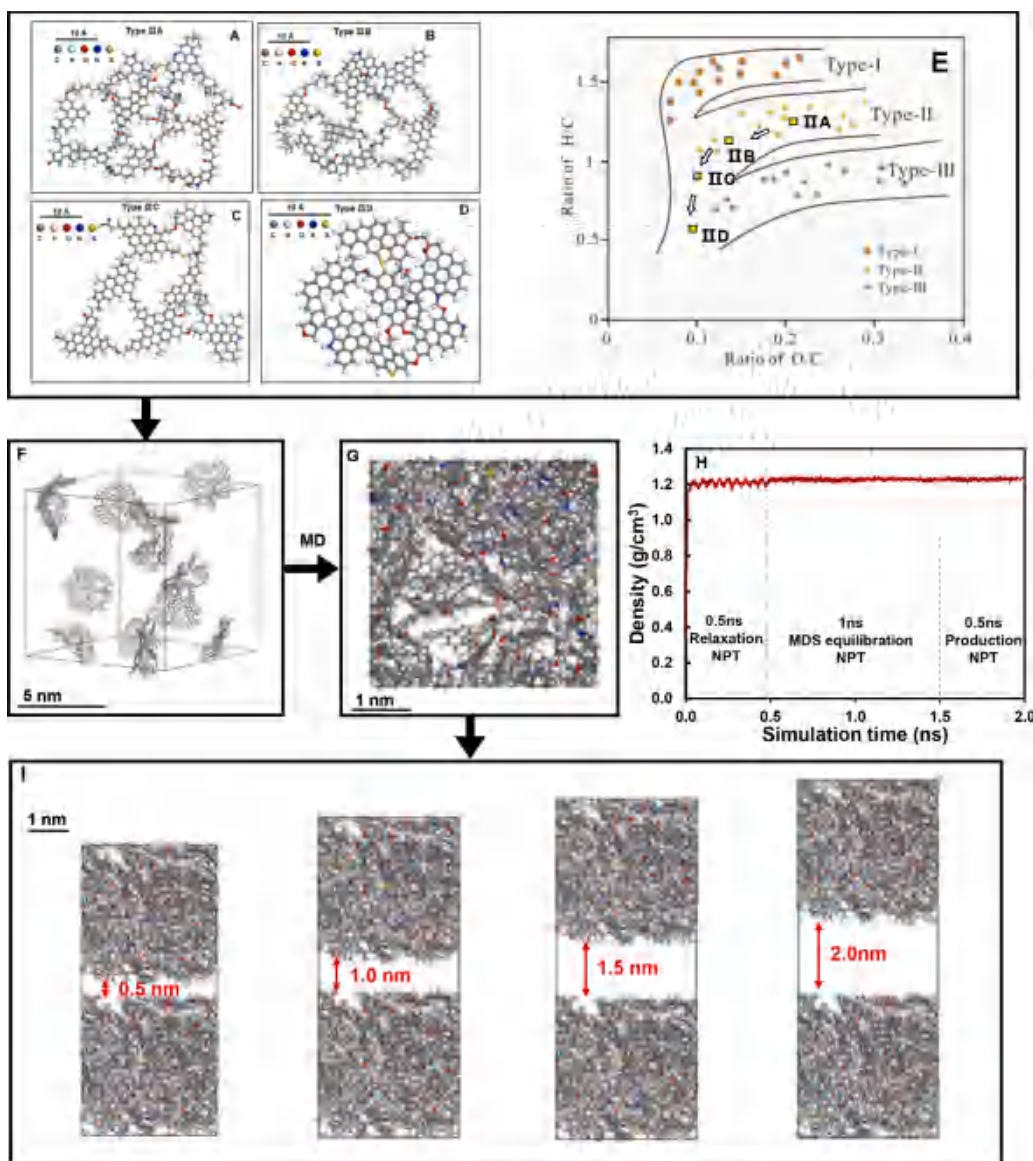


**Fig. 1.** A) The immature kerogen molecular unit (KIIA),  $C_{252}H_{294}O_{24}N_6S_3$ ; B) The early-mature (at the beginning of the oil window) kerogen molecular unit (KIIB),  $C_{234}H_{263}O_{14}N_5S_2$ ; C) The middle-late mature (at middle to end of oil window stage) kerogen molecular unit (KIIC),  $C_{242}H_{219}O_{13}N_5S_2$ ; D) The overmature (gas window) kerogen molecular unit (KIID),  $C_{175}H_{102}O_9N_4S_2$ ; E) The maturity stages of different kerogen units in Van Krevelen diagram. Modified from (Ungerer, 2015) [38] and (Kelemen, 2007) [37]; F) The KIID low density relaxed kerogen model; G) The KIID final condensed kerogen matrix model; H) The density variation of KIID kerogen in dynamic simulation with NPT ensemble; I) the KIID kerogen slit models.



### 2.3. Construction of kerogen models

Type II kerogen molecular units built by Ungerer [38] have been used in this study. The kerogen molecule units, KIIA, KIIB, KIIC, and KIID, represent immature, early-mature (beginning of the oil window), middle-late mature (middle to end of the oil window), and overmature (gas window) kerogens (Fig. 1A, B, C, and D), respectively, with the exact maturity stages shown on the Van Krevelen diagram (Fig. 1E).

Pre-optimised kerogen units were used to construct initial low density ( $0.1 \text{ g/cm}^3$ ) kerogen relaxed matrix models (Fig. 1F). The number of kerogen units (10 for KIIA, 10 for KIIB, 10 for KIIC, and 13 for KIID) (Table S1) varies depending on 1) the simulated matrix size (final kerogen cell is 3.85, 3.70, 3.68, and 3.52 nm cube, respectively) should  $> 3.1 \text{ nm}$  (twice the cut-off distance), and 2) the simulated system should be excessive regarding computational workload. Then, a series of molecular dynamic simulations were applied, Geometry Optimisation being used to obtain the local minimal energy structure of the initial kerogen matrix. A relaxation of 1 ns from  $500^\circ\text{C}$  to  $100^\circ\text{C}$  with the NVT ensemble (0.5 ns) and NPT ensemble (0.5 ns) was conducted to obtain the global minimum energy structure. After that, the 1.5 ns dynamic simulation was carried out in the NPT ensemble to derive the stable condensed kerogen matrix model (Fig. 1G). The system reaches equilibrium after a dynamic simulation time of 2.5 ns, since the equilibration of density is reached (Fig. 1H). The periodic boundary conditions were applied in X, Y, and Z directions, which consist of an infinite number of units.

Kerogen slit models with pore width sizes of  $0.5 \pm 0.2$ ,  $1.0 \pm 0.2$ ,  $1.5 \pm 0.2$ , and  $2.0 \pm 0.2 \text{ nm}$  were also constructed for the overmature kerogen (KIID) (Fig. 1I), together with KIID matrix, used to compare with the overmature isolated kerogens (K1, K2, and GH3). The slit pore width sizes were controlled by adjusting the distance between the centroids of the two kerogen matrix layers when constructing the slit models. The unevenness of the kerogen molecular structure (Fig. 1D) results in the slit pores being over the range of  $\pm 0.2 \text{ nm}$  for the stated pore size. Kerogen matrix and slit models with the increasing moisture contents (0, 0.6, 1.2, 2.4, 3.6, 6, 9, 12, 15, 18, 21, 24, 27, 30, 36 and 42 wt% TOC, where wt% TOC is the moisture weight percentage on a TOC basis) were constructed sequentially by water adsorption through Fix Loading task with GCMC method to obtain the moist kerogen models ('moist' is used to distinguish the simulated kerogens from 'wet' for the isolated kerogens used experimentally). 42 wt% TOC is the maximum moisture content that the kerogen models can contain, which is obtained on the basis of the water adsorption isotherms for the kerogen models (Figure S3). The kerogen models were built as triplicate, and the average simulation data were applied to represent the authentic results.

### 2.4. Simulation methods

#### 2.4.1. Methane adsorption by GCMC

The methane adsorption isotherms up to 300 bar were obtained by the GCMC method for the (dry and moist) simulated kerogen models at 25 and  $100^\circ\text{C}$ , since the isotherms are close to reaching equilibrium at 300 bar. GCMC simulation allows the methane to penetrate into any large enough space in the kerogen models. Fugacity was used in the GCMC simulation, which can be converted to pressure by the fugacity coefficient calculated by the Peng-Robinson equation [30,74]. A total of  $2 \times 10^7$  Monte Carlo simulation steps were performed at each pressure, with the first  $1 \times 10^7$  steps for equilibration and the second  $1 \times 10^7$  steps for production. The dual-site Langmuir (DSL) model (Equation (5)) [3] developed from classical Langmuir model is used to predict the equilibrium methane adsorption quantity ( $Q_m$ ) based on the simulation results of methane adsorption isotherms, which is the same model used for fitting and predicting experimental results on isolated kerogens [4]. The DSL model is more suitable for the heterogeneous adsorbents since two adsorption sites are considered [3]. Methane adsorption at  $25^\circ\text{C}$  for the kerogen matrix and slit models are used to compare with experimental

results.

$$Q_a(P, T) = Q_m \bullet \left[ (1 - \alpha) \frac{b_1(T)P}{1 + b_1(T)P} + \alpha \frac{b_2(T)P}{1 + b_2(T)P} \right] \quad (5)$$

where,  $Q_a$  is the absolute adsorption quantity obtained from simulation;  $Q_m$  is the max equilibrium absolute adsorption quantity;  $b_1(T)$  and  $b_2(T)$  are the temperature-dependent equilibrium constants, which are related to the energy of adsorption sites;  $b_1(T)$  and  $b_2(T)$  are weighted by a coefficient ( $\alpha$ );  $\alpha$  is the fraction of the second type of site ( $0 < \alpha < 1$ );  $P$  is the pressure;  $T$  is the temperature.

#### 2.4.2. Microporosity measurement

The micropore volume in the simulation is the Connolly volume measured by the dummy probes, the size of which can vary (Fig. 2A). The measured surface of a solid (Fig. 2B) can be defined as 1) van der Waals surface formed by the outer part of the van der Waals spheres of the surface atoms, 2) Connolly surface, which is the probe accessible surface and used in simulation studies. This is defined as the surface drawn by the bottom of a spherical probe molecule rolling over the van der Waals surface. 3) The R-distance surface is located at a distance  $R$  from the Connolly surface [60]. The corresponding pore volume is the region wrapped by the surface, and the accessible pores depend on the size and shape of the probe molecules [30,60,75]. In this simulation, the micropore size distribution (MPSD) of kerogen models is obtained by the micropore volume measured by dummy probes with different diameters ( $d$ ) from 0.10 to 2.0 nm. The dummy probes with various diameters can be compared with the gas molecules having the same kinetic diameter, such as  $d = 0.26 \text{ nm}$  for Helium (He),  $d = 0.33 \text{ nm}$  for carbon dioxide ( $\text{CO}_2$ ),  $d = 0.36 \text{ nm}$  for Nitrogen ( $\text{N}_2$ ), and  $d = 0.38 \text{ nm}$  for methane ( $\text{CH}_4$ ) [67,76,77]. The micropore volume ( $V_{\text{micro}}$ ) for simulation of dry kerogen was measured by the 0.33 nm ( $\text{CO}_2$  diameter) probe, and for moist kerogen, was measured by 0.36 nm ( $\text{N}_2$  diameter) probe, to be consistent with the results from the low-pressure gas adsorption measurements (Supplemental information, Section S1.1), where the micropore volumes of dry and wet isolated kerogens are obtained from  $\text{CO}_2$  and  $\text{N}_2$ , and  $\text{N}_2$  gas sorption, respectively, through the NLDFT model [4].

#### 2.4.3. Molecular dynamic simulation

The affinity between the water/methane molecules and different functional groups is revealed by the Radial distribution function (RDF) analysis from the MD simulation for the adsorption mechanism analysis. The relaxed kerogen matrix (Fig. 1F) was used to eliminate the pore structure effect. Different numbers (5, 10, 25, 50, 75, 100, 150, 200, 250, 300) of methane/water molecules were loaded by Fix Loading and GCMC to represent the density and pressure changes for methane ( $0.0002\text{--}0.0124 \text{ g/cm}^3$ ,  $0.3\text{--}18.5 \text{ bar}$  at  $25^\circ\text{C}$ ,  $0.4\text{--}23.6 \text{ bar}$  at  $100^\circ\text{C}$ ) and different moisture contents (0.3, 0.7, 1.7, 3.3, 5.0, 6.6, 10, 13, 17 and 20 wt% TOC) in the kerogen models (Figure S4). The relative number density ( $g(r)$ ) (Equation (6)) and the relative coordination number ( $C_r$ ) (Equation (7)) were obtained after the 2.0 ns MD simulation was carried out at  $25^\circ\text{C}$  and  $100^\circ\text{C}$  in the NVT ensemble. The first 1.0 ns was used for equilibration, and the second 1.0 ns for outputting results. The  $g(r)$  and  $C_r$  of methane and water around a specific functional group can indicate the strength of affinity, increasing values of  $g(r)$  and  $C_r$  suggesting stronger affinity.

$$g(r) = \frac{\rho_r}{\rho_{\text{cell}}} = \frac{\frac{dN}{4\pi r^2 dr}}{\frac{N}{V_{\text{cell}}}} \quad (6)$$

$$C_r = \frac{\sum dN}{N} = \frac{g(r) \bullet 4\pi r^2 dr}{V_{\text{cell}}} \quad (7)$$

where,  $g(r)$  is the relative number density,  $\rho_r$  is the number density of methane/water around the particular functional group,  $\rho_{\text{cell}}$  is the number density of methane/water in the simulation cell,  $dN$  is the amount of methane/water around the functional group when the

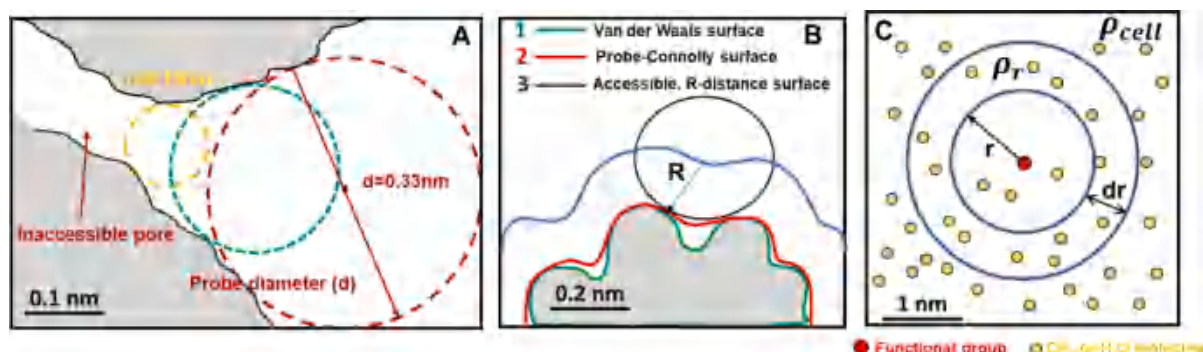


**Fig. 2.** A) Depiction of pore volume measurement by different probes, the probe diameters ( $d$ ) range from 0.1 to 2.0 nm in this study, B) diagram of van der Waals (1), Connolly probe accessible (2), and the accessible, R-distance (3) surfaces of an adsorbent (modified from (Thommes, 2015) [60]), C) diagram depicting methane or water molecules around a functional group for calculating relative number density and coordination number.

measured distance is  $r$  with the measured thickness of  $dr$  (Fig. 2C),  $N$  is the number density of methane/water in the cell,  $V_{cell}$  is the volume of the cell,  $C_r$  is the relative coordination number.

### 3. Result and discussion

#### 3.1. Model validation

TEM is an effective tool to observe the micropore structure of the amorphous organic matters, including carbon or kerogen in shale [78–81]. Here, for the isolated kerogens K1 and K2, TEM indicates the micropores of kerogen in shale comprise 1) small micropores ( $<1$  nm) inside of kerogen matrix (Fig. 3A), and 2) larger micro ( $>1$  nm), meso, or even macropore between the kerogen matrix (Fig. 3B and 3C). The small micropores ( $<1$  nm) of realistic kerogen matrix (Fig. 3A) can be represented by the kerogen matrix model (Fig. 1G), and the larger micropores ( $>1$  nm) (Fig. 3C) can be represented by kerogen slit models (Fig. 1I).

The micropore size distributions (MPSD) for dry kerogens from simulation and experiment are compared in Fig. 4. The isolated kerogens, K1, K2, and GHK3 with VRs of 2.95, 2.58, and 1.95%Ro, respectively, are in the overmature (gas window) stage, which are comparable with overmature simulated kerogen (KIID). Fig. 4A confirms that isolated kerogens contain both ultra-micropores ( $<0.7$  nm) and super-micropores (0.7–2.0 nm), with two significant peaks. The first ( $P_{ul}$ ) and second ( $P_{su}$ ) peaks are in the ranges of 0.3–0.5 nm and 0.7–2.0 nm, respectively, with GHK3 having a much smaller  $P_{su}$  peak than K1 and K2, indicating most (about 98%) of the pores in GHK3 are ultra-micropores ( $<0.7$  nm).

Three peaks are observed for the simulated kerogen micropore size distributions (Fig. 4B). The largest peak,  $P_{in}$ , ranging from 0 to 0.26 nm, arises from pores inaccessible experimentally to any gas molecule (even He). The smallest peak ( $P_{ul}$ ) (peak value  $< 10$  mm<sup>3</sup>/g TOC) (Fig. 4B) is

very close to the ultra-micropore peak ( $P_{ul}$ , peak value is 3–12 mm<sup>3</sup>/g TOC) in the isolated kerogen (Fig. 4A), ranging from 0.3 to 0.5 nm. This peak is present in all kerogen models (Fig. 4B). The third peak ( $P_{su}$ , peak value  $< 30$  mm<sup>3</sup>/g TOC) is observed for all the slit models ranging from 0.8 to 2.0 nm, depending on slit size (Fig. 4B), which is comparable with the super-micropore peaks ( $P_{su}$ , peak value  $< 12$  mm<sup>3</sup>/g TOC) in the isolated kerogens (Fig. 4A).

In summary, the MPSD of dry kerogen from experiment and simulation are comparable, where the KIID matrix and KIID 0.5 nm slit models are representative of the ultra-micropores dominating in kerogen GHK3, and the 1.0, 1.5, and 2.0 slits models containing both ultra-micropores and super-micropores which are comparable to K1 and K2.

Although kerogen structure is complex and heterogeneous, there is a relatively consistent range (1.1–1.8 g/cm<sup>3</sup>) of skeleton densities for isolated kerogen, which can be used as a criterion to validate the simulated models [6,30,54,82,83]. The skeleton densities of the isolated kerogens K1, K2, and GHK3 are 1.17, 1.83, and 1.44 g/cm<sup>3</sup>, respectively (Table 1). A range of 1.10–1.65 g/cm<sup>3</sup> for type II isolated kerogens with differing maturity has been reported in previous research [6,82–84]. The isolated kerogens could contain various denser minerals leading to a relatively higher skeleton density from the experiment than simulation [6,82,83,85], where in this simulation, the skeleton densities for the KIIA, KIIB, KIIC, and KIID matrices are 1.11, 1.12, 1.16, and 1.20 g/cm<sup>3</sup>, respectively (Table S1). A density of 1.0–1.15 g/cm<sup>3</sup> for KIIA [30,38,53,67], 1.16 and 1.18 g/cm<sup>3</sup> for KIIB and KIIC [53], and 1.18–1.28 for KIID [38,53,55,86] were reported in previous simulations, in good agreement with the matrix density obtained from this study.

In addition, the lower bulk densities (0.21 to 0.59 g/cm<sup>3</sup>) of K1, K2, and GHK3 arises from their high porosity (75–89%) (Table 1). The bulk density of kerogen slit models reduces with increased pore volume, for KIID 0.5, 1.0, 1.5, and 2.0 nm slits models being 1.12, 1.06, 1.0, and



**Fig. 3.** A) TEM image of micropores in isolated kerogen matrix (K1), B) TEM image of a mesopore in isolated kerogen matrix (K2), C) TEM image of a mesopore and micropore neck for isolated kerogen matrices (K2).

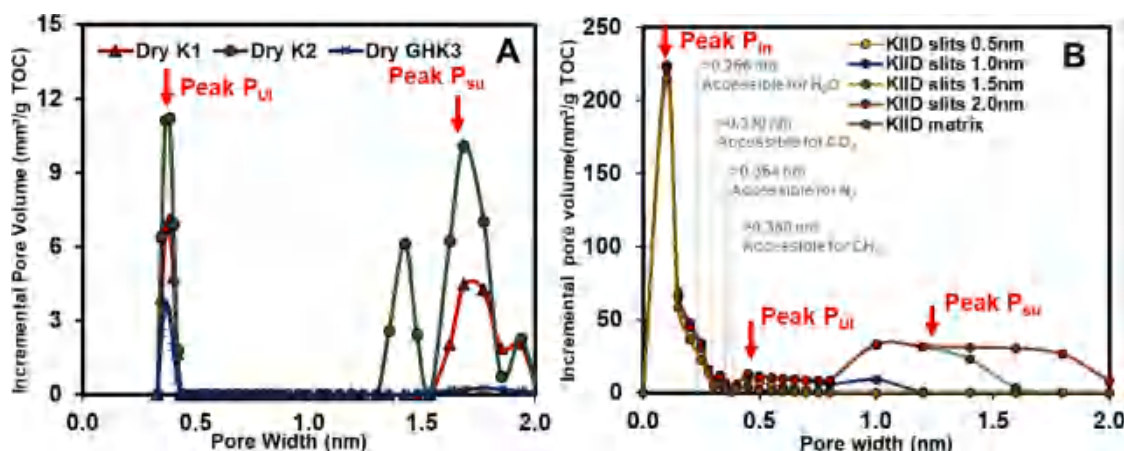


**Fig. 4.** The micropore size distributions (MPSD) of A) isolated kerogens (K1, K2, and GHK3) and B) kerogen matrix and slits models. The micropore volumes of the isolated kerogens are on a TOC basis to eliminate the impact of residue minerals.

**Table 1**

Basic parameters for the isolated kerogens used in this study.

| Kerogen name | Porosity (%) | Skeleton Density (cm <sup>3</sup> /g) | Bulk Density (cm <sup>3</sup> /g) | Dry V <sub>ultra</sub> (mm <sup>3</sup> /g TOC) | Dry V <sub>micro</sub> (mm <sup>3</sup> /g TOC) | Dry Q <sub>m</sub> (mg/g TOC) | Wet V <sub>ultra</sub> (mm <sup>3</sup> /g TOC) | Wet V <sub>micro</sub> (mm <sup>3</sup> /g TOC) | Wet Q <sub>m</sub> (mg/g TOC) | Q <sub>m</sub> reduction |
|--------------|--------------|---------------------------------------|-----------------------------------|---|---|-------------------------------|---|---|-------------------------------|--------------------------|
| K1           | 89           | 1.17                                  | 0.21                              | 24  | 39  | 75.8 ± 3.96                   | 0   | 2.7   | 19.3                          | 75%                      |
| K2           | 85           | 1.83                                  | 0.43                              | 37  | 75  | 89.6 ± 5.01                   | 0   | 5.9   | 35.1                          | 61%                      |
| GHK3         | 75           | 1.44                                  | 0.59                              | 9.8   | 10  | 21.25 ± 1.54                  | 0   | 1.2   | 6.1                           | 71%                      |

Porosity is the ratio of the total pore space divided by the total sample volume, V<sub>ultra</sub> is the ultra-micropore (<0.7 nm) volume, V<sub>micro</sub> is the total micropore (<2 nm) volume. Q<sub>m</sub> is the maximum equilibrium methane adsorption quantity, the mean of Q<sub>m</sub> is from triplicate experiments, and the errors represent the dispersion of a dataset relative to its average. The ‘wet’ in this table means the 95% R.H. moisture equilibrium isolated kerogens.

0.94 g/cm<sup>3</sup>, which is lower than the kerogen KIID matrix density (1.20 g/cm<sup>3</sup>). The bulk density of the KIID slit models (0.94–1.12 g/cm<sup>3</sup>) are larger than those of isolated kerogens (0.21–0.59 g/cm<sup>3</sup>, Table 1) since the models only represent kerogen containing certain micropores, and there are much more larger pores (*meso* and *macropores*) in isolated kerogens.

### 3.2. Impact of moisture on methane adsorption by simulation

The impact of moisture on methane adsorption capacity for the KIIA, B, C, and D matrices at 25 and 100 °C is illustrated in Fig. 5. The equilibrium methane adsorption capacities (Q<sub>m</sub>) of the dry kerogen matrices increase with maturity and decrease with temperature. The Q<sub>m</sub> for the dry KII A, B, C, D matrices are 16, 20, 28, and 46 mg/g TOC, respectively, at 25 °C, compared to the lower values of 13, 18, 21, and 36 mg/g TOC, respectively, at 100 °C (Fig. 5A and B). The same effects of maturity and temperature on methane adsorption capacity is also evident for the moist kerogens (Fig. 5A, B). Moisture has the expected negative impact on methane adsorption capacities for the kerogen matrices, the isotherms of which are presented in Figure S5. The negative effect increases with moisture content until values of 9, 12, 12, and 18 wt% TOC for KII A, B, C, D matrices, respectively, are reached where no the methane adsorption capacity remains (Fig. 5C and D).

The correlations between Q<sub>m</sub> reduction and moisture content for the kerogen matrices increase gradually until reaching plateau, and the increased curves can be divided into three regimes (I, II, III) described as ‘rapid’, ‘gentle’ and ‘slow’ stages as the increase of moisture content (Fig. 5C, D), with different slopes and knee points observed (Fig. 5C, D). The impact of a given moisture content increases with decreasing maturity going from KIID to KIIA. Although the moisture content ranges for corresponding stages can differ slightly depending upon maturity and temperature, they are approximately within the ranges 0–4 wt%

TOC, 4–8 wt% TOC, and >8 wt% TOC for ‘rapid’, ‘gentle’, and ‘slow’ stages (Fig. 5C, D). Over 50% reduction in Q<sub>m</sub> for the KII A, B, C, D matrices occurs when the moisture reaches *ca.* 4 wt% TOC. Moisture has the greatest effect on the low maturity kerogen KIIA, since more moisture is needed to occupy (adsorb and condense) in the larger micropores for the more mature kerogens.

### 3.3. Comparison between experiment and simulation for the impact of moisture on methane adsorption.

The methane adsorption capacities of the overmature kerogens from simulation and experiment at 25 °C are compared in Figs. 6 and 7. For dry kerogens, the methane adsorption isotherms for the KIID matrix and 0.5 nm slit models are Type I (a) isotherms [60], similar to that of GHK3 kerogen, since they mainly contain ultra-micropores (<0.7 nm). The isotherms for K1 and K2 kerogens are Type I (b) isotherms [60], matched well with that of the KIID 1.5 nm slit model, slightly out of range compared to the KIID 1.0 and 2.0 nm slit isotherms (Fig. 6A), considering the existence of both ultra-micropores (<0.7 nm) and super-micropore (0.7–2.0 nm) (Section 3.1). The Q<sub>m</sub> of the dry KIID matrix, 0.5, 1.0, 1.5 and 2.0 nm slit models clearly increases with pore size, from 46, 75, 95, 122, to 148 mg/g TOC (Fig. 6B). The Q<sub>m</sub> of the dry KIID matrix, 0.5, 1.0, 1.5 and 2.0 nm slit models clearly increases with pore size, from 46, 75, 95, 122, to 148 mg/g TOC, respectively (Fig. 6B). The Q<sub>m</sub> values from simulation are larger than those from experiment. As for the ultra-micropores predominated kerogens, the values of 46–75 mg/g TOC for KIID matrix and 0.5 nm slit models are about 2–3 times higher than that for GHK3 kerogen (21.25 mg/g TOC). And the Q<sub>m</sub> of ultra and super-micropores models (95, 122, to 148 mg/g TOC for KIID 1.0, 1.5 and 2.0 nm slit) are roughly up to 2 times higher than the experimental Q<sub>m</sub> values for the dry K1 and K2 (75.8, and 89.6 mg/g TOC, Table 1), due to all the pores being accessible for the GCMC method in simulation.



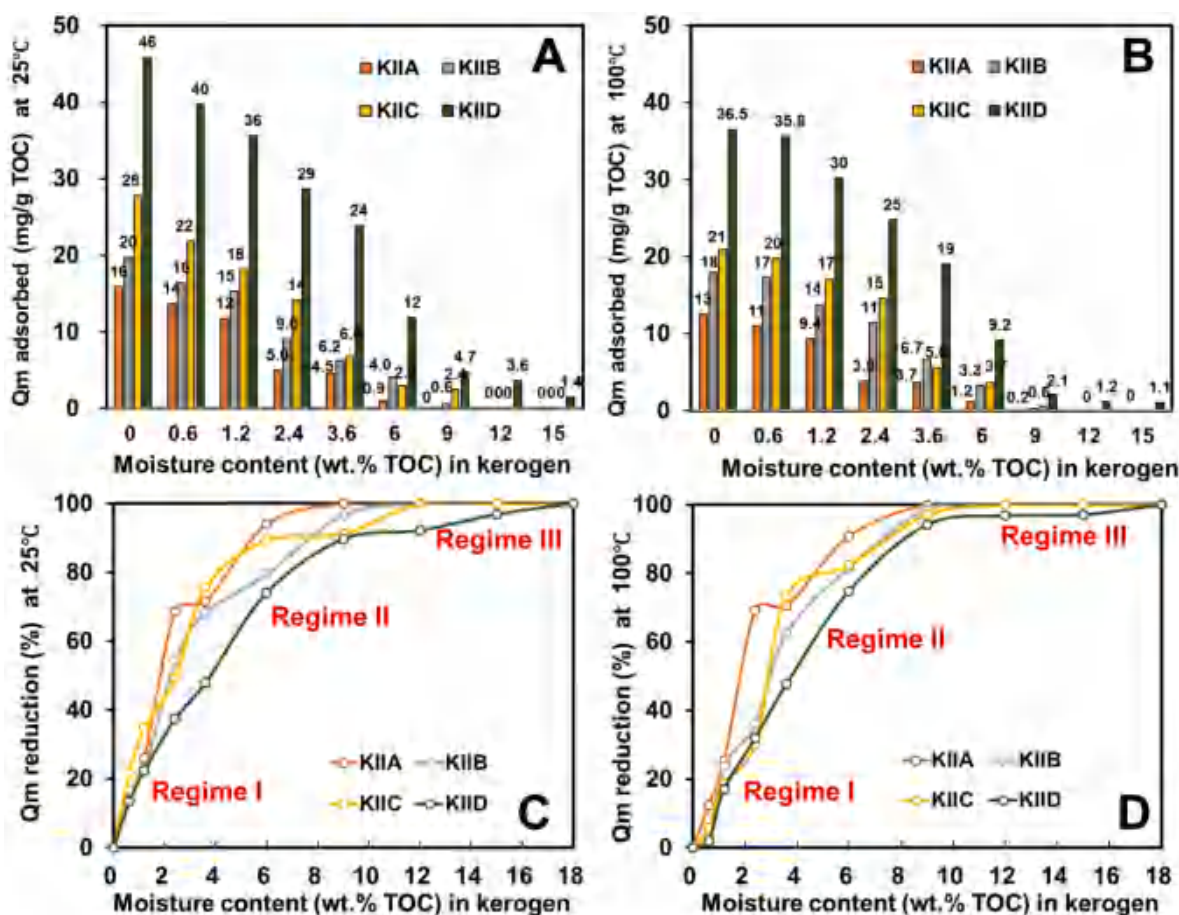


Fig. 5. The equilibrium methane adsorption capacities (Qm) of the KII A, B, C, D matrices with different moisture contents at A) 25 °C and B) 100 °C, and the Qm reductions of KII A, B, C, D matrices with different moisture contents at C) 25 °C and D) 100 °C. The Qm is calculated based on equation (5) (Section 2.4.1), and the Qm reduction is the percentage of the reduced Qm of kerogens compared to the Qm of dry kerogen. Regime I is designated the ‘rapid’ stage relating to the part of the curve with the steepest slopes, Regime II is designated the ‘gentle’ stage in the part of the curves around the knees with less steep slopes, and regime III, ‘slow’ stages refer to the curves reaching a plateau.

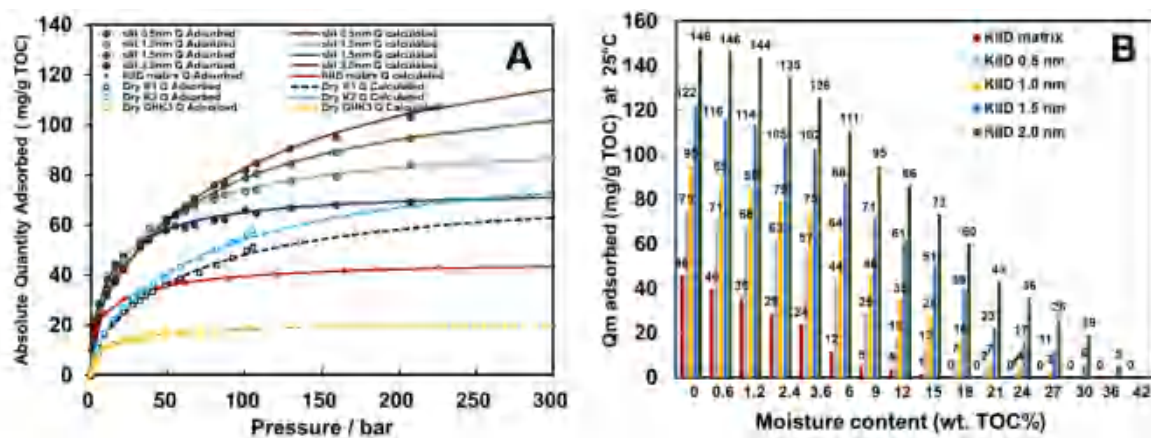


Fig. 6. A) Methane adsorption isotherms of the dry isolated kerogens and KIID models at 25 °C, B) The equilibrium methane adsorption quantity (Qm) of the KIID models with different moisture contents at 25 °C. The points ‘adsorbed’ in Fig. 6A are the measured data of methane adsorption amount from simulations and experiments, and the lines ‘calculated’ are predicted by the DSL model.

Moisture reduces the Qm by 75, 61, and 71% for K1, K2, and GHK3, respectively (the Qm for wet isolated kerogens being 19.3, 35.1, and 6.1 mg/g TOC, respectively, (Table 1). The Qm of the KIID models with different moisture contents (0–42 wt% TOC) obtained by GCMC simulation at 25 °C are presented in Fig. 6B. The moist kerogen structures

lose all their methane adsorption capacity when the moisture contents are 18, 27, 30, 36, to 42 wt% TOC for the KIID matrix, 0.5, 1.0, 1.5, and 2.0 nm slit models, respectively, indicating more moisture is required with increasing pore size (Fig. 6B).

The Qm reduction for the kerogen slit models (Fig. 7A) can be

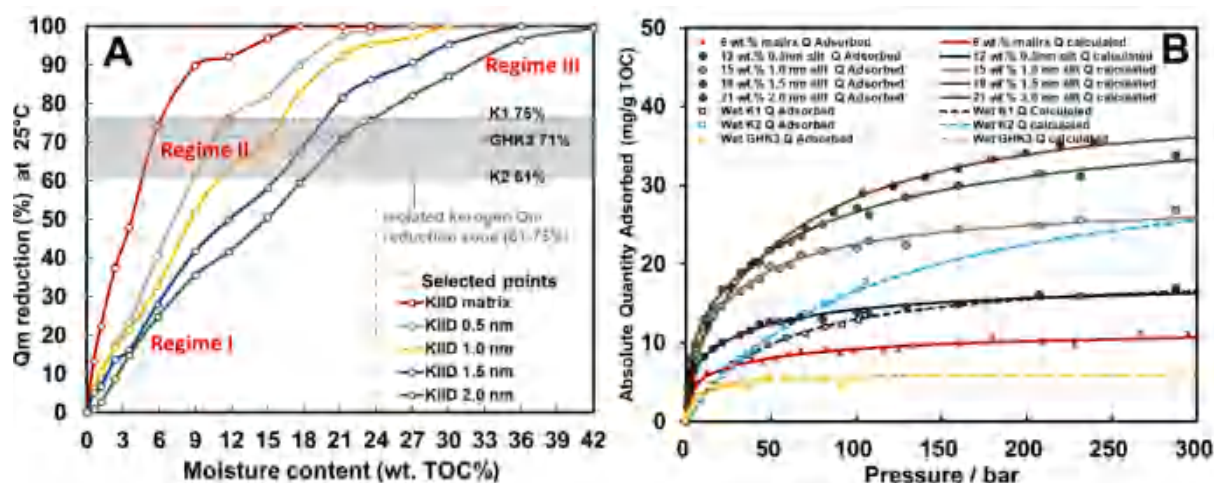


Fig. 7. A) Qm reduction for the KIID matrix, 0.5, 1.0, 1.5, and 2.0 nm slit models with the different moisture contents at 25 °C, B) Methane adsorption isotherms of wet isolated kerogen and moist KIID models at 25 °C. The points ‘adsorbed’ in Fig. 7B are the measured data of methane adsorption amount from simulations and experiments, and the line ‘calculated’ is predicted by the DSL model. Regime I is designated the ‘rapid’ stage relating to the part of the curve with the steepest slopes, Regime II is designated the ‘gentle’ stage in the part of the curves around the knees with less steep slopes, and regime III, ‘slow’ stages refer to the curves reaching a plateau.

divided into ‘rapid’, ‘gentle’, and ‘slow’ stages as for the kerogen matrices (Fig. 5), with the changes from ‘rapid’ to ‘gentle’ stages being less evident with increasing pore size (Fig. 7A). The experimental results reveal similar effects for the Qm versus moisture content plot exhibiting a linear decreasing stage, a flat stage, and then a convex decreasing stage [87]. To find the representative moist kerogen models for the 95% R.H wet isolated kerogens, the Qm reductions (61–75%) of wet isolated kerogens are marked in Fig. 7A. The moist KIID kerogen (matrix, 0.5, 1.0, 1.5, and 2.0 nm slit) models across a moisture content range of 4–24 wt% TOC are selected as the representative moist models, as same Qm reductions for wet isolated kerogen are observed (Fig. 7A). Whereas, the moisture contents of 4 to 24 wt% TOC for kerogen micropore models from the simulation are less than the moisture contents (70, 43, and 38 wt% TOC for K1, K2, and GHK3) measured for wet (95%R.H.) isolated kerogens, suggesting that not all the moisture is in the micropores of isolated kerogens.

The methane adsorption isotherms of the moist KIID matrix, 0.5, 1.0, 1.5, and 2.0 nm slit models with moisture contents of 6, 12, 15, 18, and 21 wt% TOC, respectively, have been selected to compare with the experimental results (Fig. 7B). The Qm reductions for moist KIID matrix and 0.5 nm slit models at 6 and 12 wt% TOC are 74% and 76%, are comparable to that (71%) for the wet GHK3 kerogen. Similarly, the Qm reductions for the moist KIID 1.0, 1.5, and 2.0 nm slit models at 15, 18, and 21 wt% TOC are 70%, 68% and 71%, which are comparable to the average Qm reduction (68%) for the wet K1 and K2 kerogens (Fig. 7A).

Similar to the dry kerogens, the Qm of the moist kerogens from simulation are higher than those of the wet kerogens from experiment (Fig. 7B). The methane adsorption isotherms of the moist KIID matrix (6 wt% TOC) and 0.5 nm slit (12 wt.%TOC) models are comparable to those for the wet GHK3 kerogens, all being Type I (a). In contrast, the isotherms for the wet K1 and K2 kerogens are Type I (b), similar to those of the moist KIID 1.0 nm (15 wt.%TOC), 1.5 nm (18 wt.%TOC), and 2.0 nm (21 wt.%TOC) slit models (Fig. 7B). However, how moisture affects the methane adsorption capacity of kerogens in simulation is slightly different from experiment. For the isolated kerogens, moisture reduces the methane adsorption capacity by taking up the pore space directly, or/and blocking the narrow pore necks (<1.3 nm) to hinder the methane migration [4], while for the simulated kerogens, moisture can only reduce the methane adsorption by occupying the available pore space, since all the pores (even closed pores) can be accessed by methane molecules in the GCMC simulation. Therefore, the same amount of

moisture should have a greater effect on the isolated kerogens than the simulated kerogens. Thus, at most, 24 wt% TOC moisture being in the wet (95%R.H.) isolated kerogen micropores, with the rest in larger pores.

### 3.4. Comparison of experiment and simulation for the impact of moisture on microporosity

The micropore characteristics for the overmature kerogen (KIID) from simulation are defined by  $d = 0.33$  nm (same as CO<sub>2</sub> used for dry isolated kerogen) and  $d = 0.36$  nm (same as N<sub>2</sub> used for wet isolated kerogen) probes (Table S2), in order to compare with the results for isolated kerogens from low-pressure gas (N<sub>2</sub> and CO<sub>2</sub>) sorption experiment. The experimental results indicate that the reductions in micropore volume of 93, 92, and 88% occur for the wet (95%R.H.) K1, K2, and GHK3 kerogens, from 39, 75, 10 mm<sup>3</sup>/g TOC to 2.7, 5.9, and 1.2 mm<sup>3</sup>/g TOC, respectively (Table 1). The negative impact of moisture on micropores is also found in simulation, with the micropore volume decreasing with increasing moisture content (Fig. 8), where the

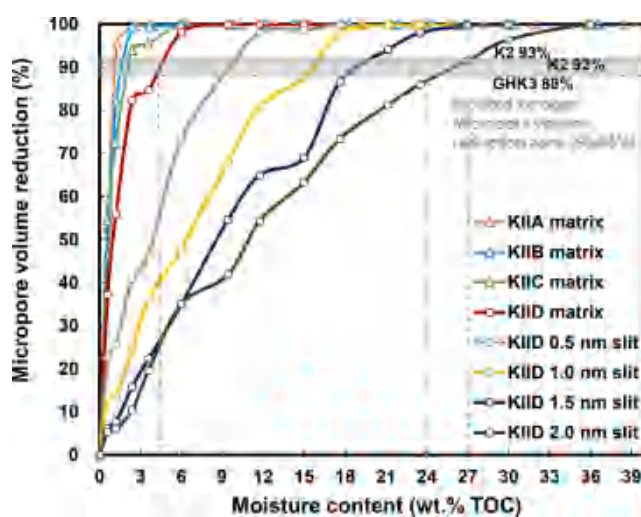


Fig. 8. Reductions in micropore volume for the kerogen (KIIA, B, C, and D) matrix and KIID 0.5, 1.0, 1.5, and 2.0 nm slit models with increasing moisture content.



micropore volume decreases fast at first and then becomes stable with increasing moisture content. The same moisture content has a greater impact on kerogen models with smaller and less pores (Fig. 8), since these pores are more easily taken up by water. All micropores ( $d = 0.36$  nm) are lost when the moisture contents are 6, 9, 12, 15, 24, 30, 33, and 36 wt% TOC for the KIIA, KIIB, KIIC, KIID, KIID 0.5 nm slit, KIID 1.0 nm slit, KIID 1.5 nm slit, KIID 2.0 nm slit models, respectively (Fig. 8).

As stated in Section 3.3, when the moisture content is in the range of 4–24 wt% TOC for the kerogen models, the same Qm reduction (61–75%) is obtained as for 95%R.H. wet isolated kerogens (Fig. 7), with the micropore reduction being around 85% (Fig. 8), slightly lower than the micropore reductions (88–93%) for wet (95%R.H.) isolated kerogens. The relatively close reduction of methane adsorption capacity (61–75%) and microporosity (85%) at the same moisture content suggests that the accessible micropore volume is the main controlling factor for methane adsorption capacity. More moisture (4–27 wt% TOC, cf. 4–24 wt% TOC) is needed for the kerogen models to reach the same micropore reduction (88–93%) than for the wet (95%R.H.) isolated kerogen (Fig. 8). However, the micropore volumes for wet isolated kerogens are measured at  $-196$  °C by  $N_2$ , where water becomes ice and can potentially block more micropores [4]. The results further indicate the moisture in wet isolated kerogens (38–70 wt% TOC) is distributed in micropores as well as larger pores, with at most 56% moisture (24 wt% TOC in micropores for K1 and K2, and 12 wt% TOC for GHK3).

Fig. 9 compares the MPSD results for wet/moist kerogens from experiment and simulation. All ultra-micropores ( $<0.7$  nm), as well as the super-micropores (0.7–2.0 nm)  $<1.3$  nm, are lost experimentally for the wet isolated kerogen [4], leaving one prominent micropore peak ranging from 1.3 to 2.0 nm (Fig. 9A). Unlike the experimental results, not all the pores  $<1.3$  nm are lost when the moisture is in the range of 4–24 wt% TOC for the KIID matrix and slit models (Fig. 9). As for the dry simulated kerogens, there are two peaks ( $P_{in}$  and  $P_{ul}$ ) for the moist kerogen matrix and 0.5 nm slit models (Fig. 9B and C), including the

inaccessible and ultra-micropore ( $<0.7$  nm). Three peaks ( $P_{in}$ ,  $P_{ul}$ , and  $P_{su}$ ) are observed for the moist kerogen 1.0, 1.5, and 2.0 nm slit models (Fig. 9D, E, and F), covering the inaccessible, ultra ( $<0.7$  nm) and super-micropores (0.7–2.0 nm). Although all the MPSD for the moist kerogens in Fig. 9 display a prominent peak for the inaccessible pores (pore size  $<0.26$  nm), these pores are not accessible for any molecule, even He, (diameter is 0.26 nm), which is the same as for the inaccessible pores in the dry kerogens as discussed in Section 3.1 (Fig. 4). Both ultra- ( $<0.7$  nm) and super-micropores (0.7–2.0 nm) exist for moist KIID slit models, and increasing moisture content simultaneously reduces  $P_{ul}$  and  $P_{su}$  (Fig. 9 D–F), suggesting moisture reduces the ultra- ( $<0.7$  nm) as well as super-micropore (0.7–2.0 nm) volume simultaneously.

### 3.5. Mechanistic description of the impacts of moisture

#### 3.5.1. Microporosity

The moisture contents of the isolated kerogens at different relative humidities (10, 30, 70, and 95%R.H.) are presented in Fig. 10, which shows the gentle increase in the lower humidity range ( $<30\%$ R.H.) for K1, K2, and GHK3 (stage 1), followed by a rapid rise in the higher humidity range for K2 and GHK3 (stage 2), with K1 reaching a plateau at the highest humidity. The maximum moisture contents of K1, K2, and GHK3 are 15.5, 13, and 9.9 wt%, corresponding to 43, 70, and 38 wt% TOC, respectively at 95%R.H. (Fig. 10). At 30%R.H., the isolated kerogen moisture contents are in the range of 7.5–17.6 wt% TOC, close to the estimated moisture contents in the micropores of kerogen simulated models (4–24 wt% TOC) (Section 3.4). Therefore, stage 1 could be due to water adsorbing/condensing in micropores first. Stage 2 at higher relative humidities could arise from water starting to fill and condense in the larger pores. Similar moisture uptake stages have been reported [26], where it was considered that the ‘gentle increase stage’ could be related to the monolayer adsorbed water, and the rapid increase could associate with the multiple layer and condensation of water. Fisher

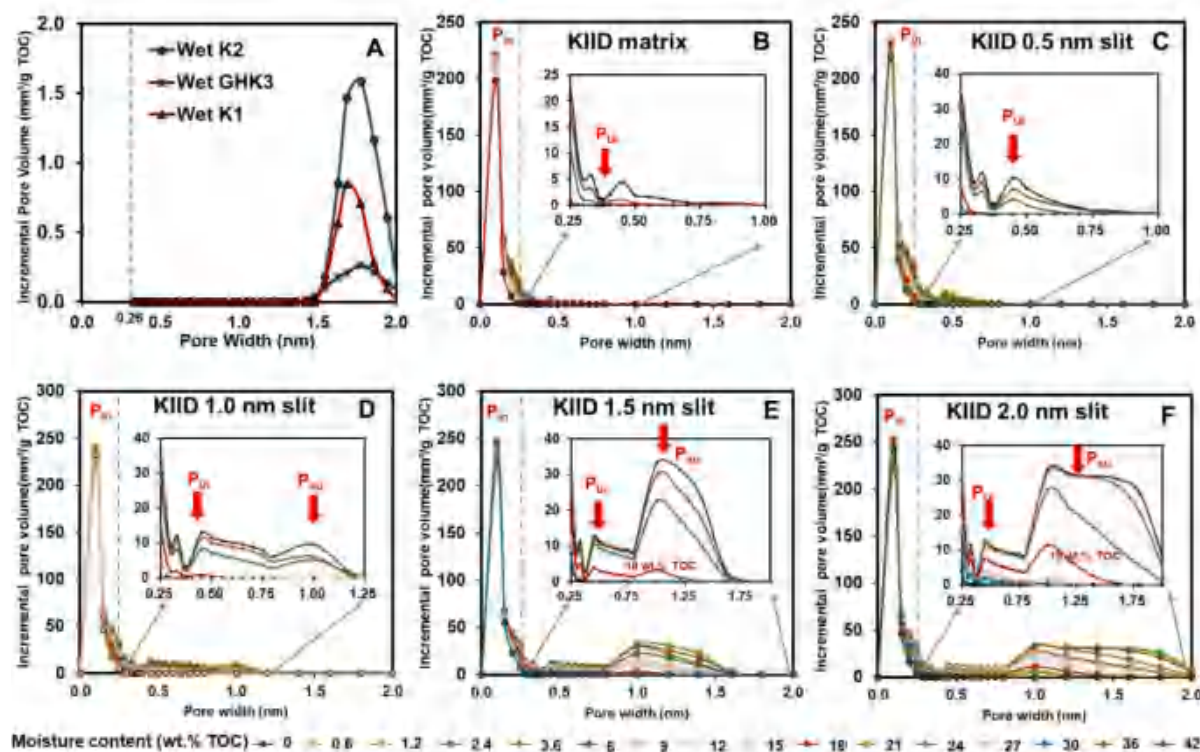


Fig. 9. The MPSD of wet (95%R.H.) isolated kerogen (A) and the MPSD of moist KIID kerogen matrix (B), 0.5 nm (C), 1.0 nm (D), 1.5 nm (E), and 2.0 nm (F) slit models at varying moisture content (wt.% TOC). The enlarged MPSD in figure B–F includes the selected moisture content from 0, 2.4, 6, 18, 24, 27, 30, and 42 wt% TOC to make the MPSD clear.

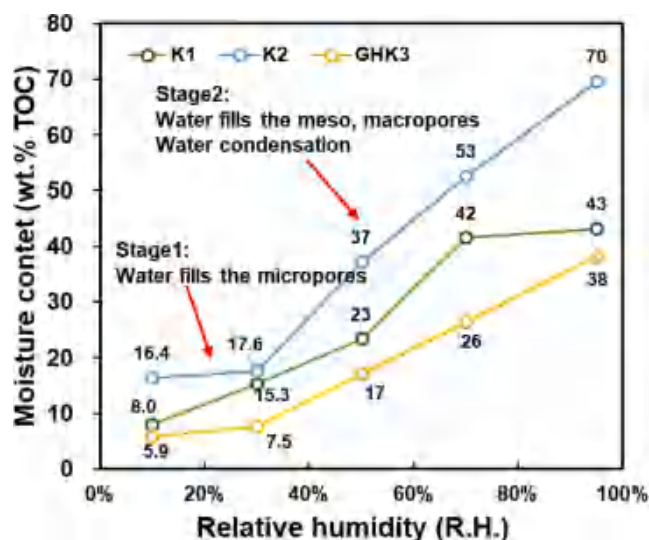


Fig. 10. The moisture contents of isolated kerogens (K1, K2, and GHK3) at different relative humidity conditions.

(1979), Fan (2018), and Wang (2018) [72,87,88] state that water condensation may occur in the larger pores following adsorption in the smaller pores, as water occupies the micropore first.

Based on the MD simulation results, the snapshots of the water distributions in the kerogen 2.0 nm slit model at different moisture contents are presented in Fig. 11. First, water adsorbs in the ultra-micropores (<0.7 nm) (Fig. 11A), and then starts adsorbing on the surface of super-micropores (0.7–2.0 nm) and filling the ultra-micropore (<0.7 nm) simultaneously (Fig. 11B). Next, water condenses and forms the water cluster (Fig. 11C and D), and finally blocks all the micropores (Fig. 11E). The same results were also obtained from the MPSD of KIID

models (Fig. 9), where all the ultra-micropores (<0.7 nm) in the KIID matrix model can be filled when the moisture content is 18 wt% TOC (Fig. 9B), but not all the ultra-micropores (<0.7 nm) are lost in KIID slit models at the same moisture content (Fig. 9E and F). This indicates that although water adsorbs in ultra-micropores (<0.7 nm) first, water will fill the ultra-micropores and start adsorbing and condensing in the super-micropore (0.7–2.0 nm) simultaneously as the moisture content increases, as opposed to filling all ultra-micropores (<0.7 nm) completely before adsorbing/filling the super-micropores (0.7–2.0 nm).

Moreover, the reduction in super-micropore (0.7–2.0 nm) volume is larger than that for ultra-micropores (<0.7 nm) at 18 wt% TOC moisture, for the KIID models with larger pores (1.5 and 2.0 nm slits, Fig. 9E and F), which confirms water preferentially condensing in super-micropores (0.7–2.0 nm) rather than continuing to fill the remaining ultra-micropores (<0.7 nm) at higher moisture contents, possibly related to the strong hydrogen-bonding between water molecules. Fig. 11F indicates that the pore connectivity is the main difference between simulation and experiment, where the blocked pores are inaccessible for methane in the experiment but accessible in the GCMC simulation.

### 3.5.2. The impact of functional groups for moist kerogen

The main compositional differences in kerogens are controlled by various functional groups, where, with increasing maturity, kerogen loses many O, N, S, and aliphatic C functional groups due to the generation of hydrocarbons (Table S3) [37,38]. KIIA, as the immature kerogen, includes all kinds of functional groups, as shown in Fig. 12.

The affinities between water/methane molecules and the functional groups are represented by the relative coordination number ( $C_r$ ) from MD simulation, with the immature kerogen KIIA, and overmature KIID selected for comparison (Figs. 13 and 14). The results for the other models (KIIB and KIIC) are in Figures S6 and S7. The affinity of methane is related to pressure and temperature (Fig. 13). At 25 °C, the  $C_r$  of methane for most functional groups are in the range of 0.002–0.008 at

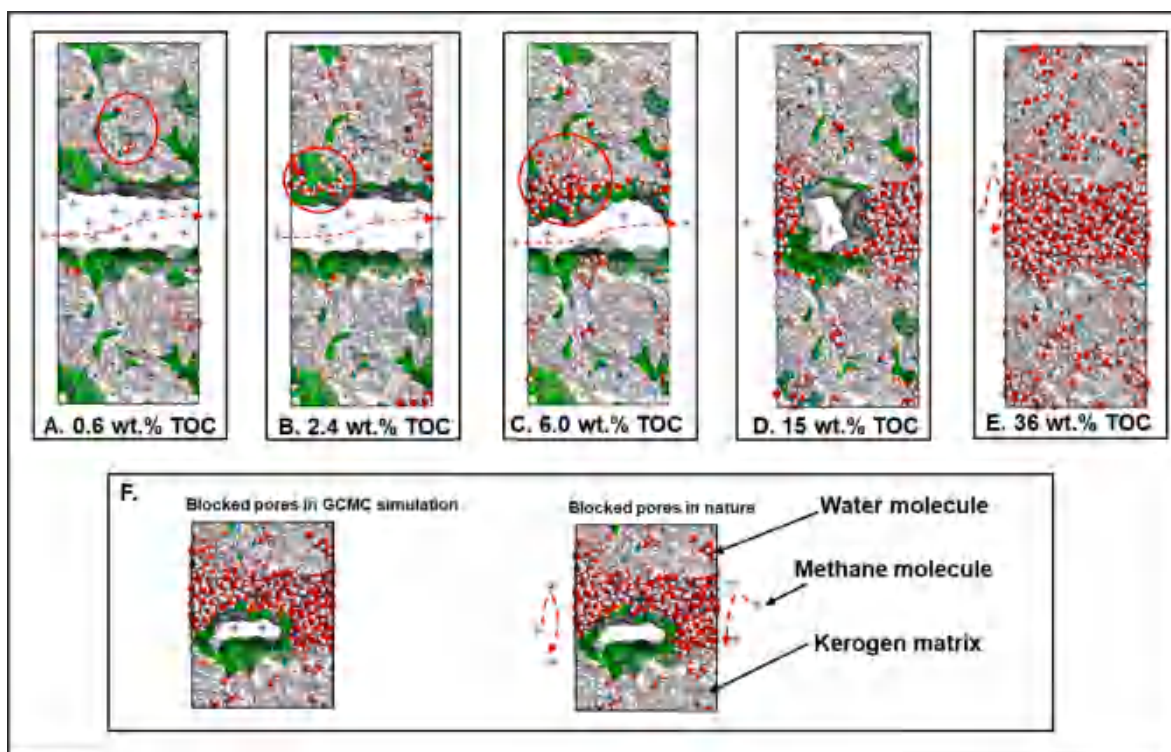


Fig. 11. Depiction of how water reduces methane adsorption capacity by filling the microporosity in the 2.0 nm slits for the KIID kerogen model. The green area is the area detected by a 0.36 nm diameter probe ( $N_2$ ), the ultra-micropores are mainly inside of the kerogen matrix layers, and the super-micropores are the pores space between the matrix layers.



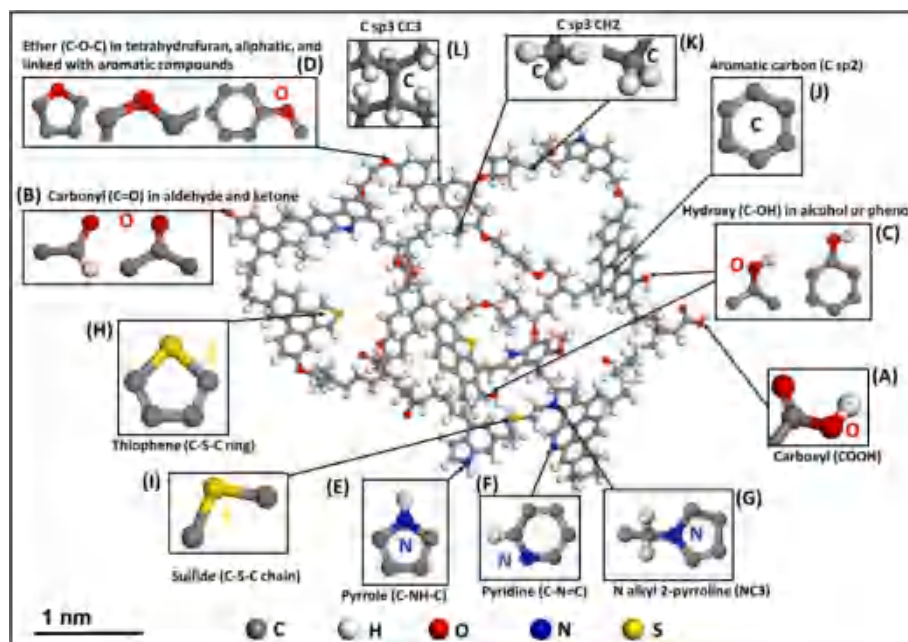


Fig. 12. Examples of the functional groups in the KIIA molecular structure.

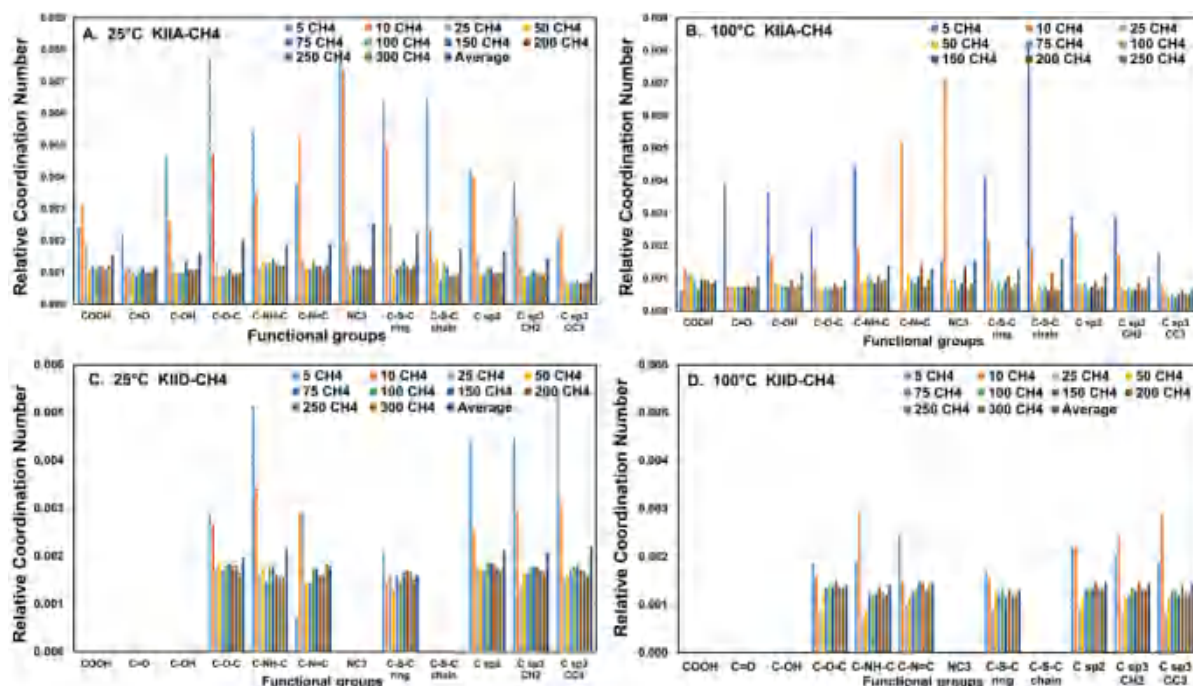
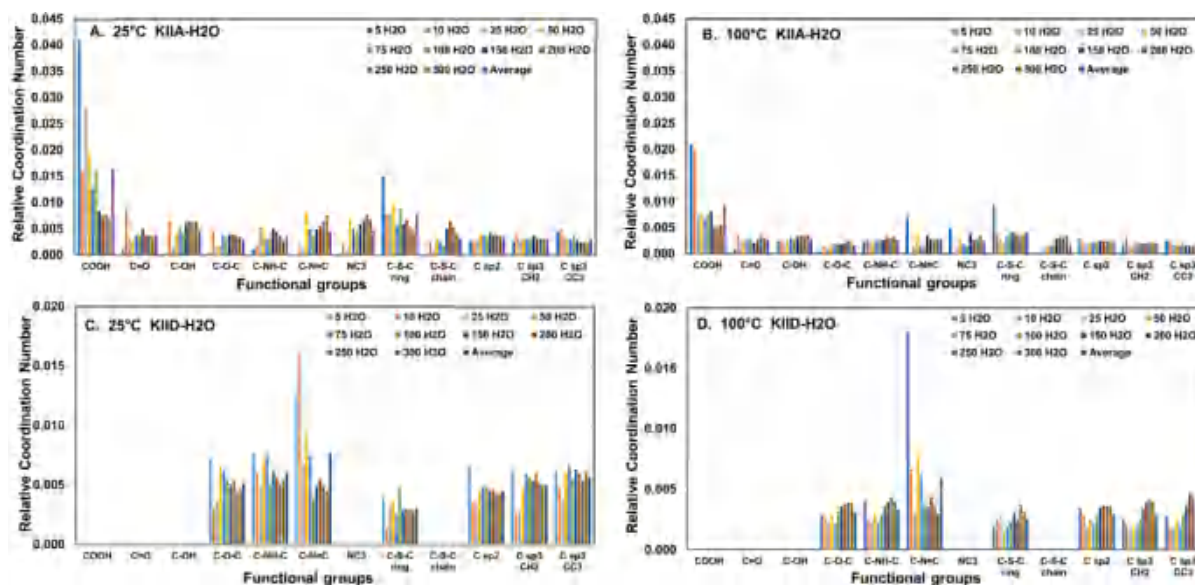


Fig. 13. The relative coordination number ( $C_r$ ) of methane ( $\text{CH}_4$ ) for the different functional groups in kerogen (KIIA and KIID) at 25 °C and 100 °C. 'Average' is the average  $C_r$  of methane going from 5 to 300 methane molecules. A) KIIA at 25 °C, B) KIIA at 100 °C, C) KIID at 25 °C, D) KIID at 100 °C.

low methane amount/pressure (<25  $\text{CH}_4$ , <1.6 bar, at 25 °C) conditions (Fig. 13). As the amount of methane and pressure increase (>25  $\text{CH}_4$ , >1.6 bar, at 25 °C), the lower  $C_r$  are observed (Fig. 13A and C), all <0.0015, which indicates that the affinity of methane with these functional groups is weaker and shows no significant differences at higher pressures. The higher temperature leads to lower  $C_r$  (Fig. 13B and D). Furthermore, the average  $C_r$  of methane with different functional groups for KIIA, KIIB, KIIC, and KIID are combined further to present the selectivity of methane (Fig. 15). The average  $C_r$  of methane for the different functional groups are very close (Fig. 15), as expected, confirming preferred sorption sites exist.

The average  $C_r$  of water for most functional groups (except COOH for KIIA) is close to 0.005 at 25 °C, and 0.003 at 100 °C, for both KIIA and KIID (Fig. 14), much higher than those for methane (<0.0015) (Fig. 13), confirming that water, being polar, has a stronger affinity than methane with all the functional groups in kerogen. Further, the changes in water content have different impacts on affinity compared to methane. At low moisture content (<10  $\text{H}_2\text{O}$ , <0.7 wt.TOC) in KIIA (Fig. 14 A and B), the  $C_r$  of water for specific functional groups like COOH and C—S—C ring are higher than the  $C_r$  for other functional groups (C=O, C-OH, C—O—C, C-NH-C, C-N=C, NC3, C—S—C chain). Even lower  $C_r$  of water is observed for the remaining functional groups (C sp2, C sp3  $\text{CH}_2$ , and C





**Fig. 14.** The relative coordination number ( $C_r$ ) of water ( $H_2O$ ) for the different functional groups in kerogen (KIIA and KIID) at 25 °C and 100 °C. ‘Average’ is the average  $C_r$  of methane over the range 5 to 300 methane molecules. A) KIIA at 25 °C, B) KIIA at 100 °C, C) KIID at 25 °C, D) KIID at 100 °C.

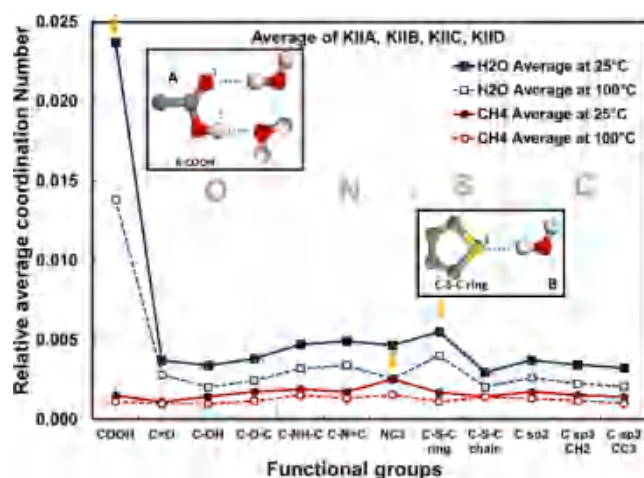


**Fig. 15.** The relative average coordination number of methane and water in the KIIA, KIIIB, KIIIC, and KIIID kerogen models over the range of 5 to 300 molecules.

sp3 C<sub>CC2</sub>) with only minor variations. This trend reflects the selective behaviour of water at low moisture contents in KIIA, which contains the widest array of functional groups. Whereas, with increasing moisture content, water starts condensing to form clusters (Fig. 11), so the  $C_r$  is not only controlled by the interaction between water and functional group but also is impacted by the H-bonding interactions between water molecules themselves. For the overmature kerogen (KIID), the  $C_r$  of water for some N-containing functional groups like C-NH-C and C-N=C at low moisture content (<10H<sub>2</sub>O, <0.7 wt.TOC) are slightly higher than those at higher moisture contents, these all being higher than the  $C_r$  of water for C-containing functional groups (Fig. 14C and D). This suggests in overmature kerogens, the lack of O and S- containing functional groups makes the N- containing groups the preferred sorption sites. However, the  $C_r$  of water for all functional groups in KIID is very close (0.005 at 25 °C, and 0.003 at 100 °C) at higher moisture contents due to the formation of water clusters, suggesting the preferred sorption sites in N-containing functional groups for overmature kerogen make little difference for water adsorption.

The average  $C_r$  of water for all functional groups in KIIA, KIIB, KIIC, and KIID at 25 °C and 100 °C (Fig. 15) shows that  $C_r$  of water for COOH

is highest, followed by the S-containing functional groups, especially cyclic C—S—C and N-containing functional groups. Although the average  $G_r$  at 100 °C is lower than that at 25 °C, the strongest affinity of water is still with COOH (Fig. 15), the increase in temperature only leading to weaker affinity.

### 3.5.3. Discussion on the combined effects of microporosity and functional groups on water and methane adsorption

A smaller pore size would enhance water adsorption for a given adsorption site, due to its higher adsorption potential, according to the potential theory of Polanyi [89]. The adsorption of water can be divided into primary and secondary sorption [23,90]. Water adsorbed on kerogen directly is the primary adsorption (monolayer), which is directly related to the ultra-micropores ( $<0.7$  nm), number and type of the preferred functional groups. Secondary sorption is multi-layer adsorption and condensation of water. The increase of moisture content will not affect the primary adsorption once all these primary sites are adsorbed by water, which mainly occurs at extremely low moisture contents (Fig. 11A and B). In comparison, the adsorption on secondary sites is directly related to the pre-adsorbed water. The adsorption and condensation of water on secondary sites is limited by the available pore space (Fig. 11 C, D, and E) rather than the preferred functional groups. Water adsorption on the secondary sites would increase with moisture content until all the pores are filled. The higher maturity samples potentially contain a more restricted distribution of functional groups and more micropores. The larger equilibrium moisture content in the over mature kerogen (Fig. 5) proves that microporosity has a stronger effect than the functional groups on water adsorption.

The dynamic behaviour of water in kerogens with increasing moisture content can be divided into four stages, considering the combined effects of microporosity and functional groups. The effect of each stage on methane adsorption related to the Qm 'rapid', 'gentle' and 'slow' reduction is explained.

Stage (a) water molecules adsorb on the primary sites of preferred functional groups in ultra-micropores ( $<0.7$  nm) or adsorbed on the ultra-micropore ( $<0.7$  nm) if no preferred functional groups are found, correlated to the monolayer water adsorption in ultra-micropores ( $<0.7$  nm) (Fig. 11 A).

Stage (b) water starts to adsorb on the primary sorption sites of the super-micropores (0.7–2.0 nm) or adsorbs on the secondary sites (pre-adsorbed water) in ultra-micropores ( $<0.7$  nm), reducing both ultra and

super-micropore (Fig. 11 B), correlated to the monolayer adsorption in super-micropores (0.7–2.0 nm), and multi-layer water adsorption/condensation in ultra-micropores (<0.7 nm) (Fig. 11B). During stage (a) and (b), water occupying (adsorbing and condensing) in ultra-micropores (<0.7 nm) and starting adsorbing in super-micropores (0.7–2.0 nm), reducing methane adsorption space directly, which lead to the ‘rapid’ Qm reduction in Fig. 5 C, D, and Fig. 7 A at low moisture contents stage.

Stage (c), water keeps adsorbing on all the secondary sites by H-bonds (Fig. 11C, D), multi-layer adsorption forming water clusters, in all the micropores. As a result, the water clusters in stage (c) reduce the methane adsorption space (for simulated and isolated kerogens) and affects their migration (for isolated kerogens), which is related to the ‘gentle’ Qm reduction stage.

Stage (d) water keeps condensing as larger clusters until all the available pores are filled (Fig. 11 E). In this stage, the constantly increasing water can fill the remainder of the less accessible pores for methane, having little impact on the methane adsorption, which correlates to the ‘slow’ Qm reduction in Fig. 5C, 5D, and Fig. 7A.

For isolated kerogens, the effects of water clusters blocking pore necks can lead to a larger Qm reduction than for simulated kerogens, which could be even more evident than the ‘gentle’ Qm reduction stage. In addition, the pore volume occupied by water is hard for methane to access, as the water adsorbed on the primary or secondary sites controlled by H-bonds which is stronger than the van der Waals interactions for methane molecules.

In earlier work, water was believed to reduce methane adsorption by a combination of affecting the microporosity as well as reducing the number of potential adsorption sites for methane or by directly occupying polar adsorption sites that would otherwise be available for methane [24,26,87,91,92]. These studies assumed that there were preferred sorption sites for methane. However, the results from this research indicate that there are only preferred sorption sites for water but not for methane. Water can thus affect methane adsorption by occupy or/and blocking the available microporosity for methane rather than completely occupy the sorption sites available for methane.

#### 4. Conclusions

- 1) The negative impact of water on methane adsorption capacity can be divided into ‘rapid’, ‘gentle’ and ‘slow’ three stages as the increase of moisture. A range of 4–24 wt.%TOC moisture content is needed for KIID matrix and slit models to reach the same reduction of Qm (61–75%) and  $V_{\text{micro}}$  (88–93%) as 95%R.H. (wet) isolated kerogens. At most, 56% of moisture in wet isolated kerogen is stored in micropores. The relatively close reduction of methane adsorption capacity and microporosity at the same moisture content suggests accessible microporosity volume is the main controlling factor for methane adsorption.
- 2) Water has a much stronger affinity with functional groups than methane. Preferred sorption sites exist for water but not for methane at reservoir conditions. Thus, the preferred sorption sites directly control water primary/monolayer adsorption at the low moisture contents, while the pore volume limits the water secondary adsorption (multiple-layer or condensation).
- 3) Ultra-micropores (<0.7 nm) are the primary pores responsible for water adsorption at low moisture contents. Water then fills the ultra- (<0.7 nm) and super-micropore (0.7–2.0 nm) simultaneously as moisture content increases.
- 4) Water occupying (adsorbing and condensing) ultra-micropores (<0.7 nm) and starting adsorbing super-micropores (0.7–2.0 nm) reduces methane adsorption space directly, leading to the ‘rapid’ Qm reduction stage at extremely low moisture contents. The condensed water clusters in most micropores can relate to the ‘gentle’ Qm reduction stage. Water fills the remaining less accessible pores for methane at higher moisture contents, having little impact on the

methane adsorption, which correlates to the ‘slow’ Qm reduction stage. Therefore, water affects methane adsorption by occupying or blocking the available microporosity for methane rather than occupying the preferred sorption sites.

#### Declaration of Competing Interest

The authors declare that they have no known competing financial interests or personal relationships that could have appeared to influence the work reported in this paper.

#### Data availability

Data will be made available on request.

#### Acknowledgements

The authors greatly acknowledge financial support from the Natural Environment Research Council (Grant no: NE/C507002/1), the Faculty of Engineering Research Excellence Ph.D. Scholarship for Wei Li provided by the University of Nottingham, and the research grants of the Horst and Jessie von Bandat Memorial Grant provided by The American Association of Petroleum Geologists (AAPG) Foundation. The British Geological Survey is acknowledged for providing the cores for the UK shales.

#### Appendix A. Supplementary data

Supplementary data to this article can be found online at <https://doi.org/10.1016/j.cej.2022.139942>.

#### References

- [1] J.B. Curtis, Fractured shale-gas systems, AAPG Bull. 86 (11) (2002) 1921–1938.
- [2] R.J. Ambrose, R.C. Hartman, M. Diaz-Campos, I.Y. Akkutlu, C.H. Sondergeld, Shale gas-in-place calculations part I: new pore-scale considerations, SPE J. 17 (01) (2012) 219–229.
- [3] X. Tang, N. Ripepi, N.P. Stadie, L. Yu, M.R. Hall, A dual-site Langmuir equation for accurate estimation of high pressure deep shale gas resources, Fuel 185 (2016) 10–17.
- [4] W. Li, L.A. Stevens, C.N. Uguna, C.H. Vane, W. Meredith, L. Tang, Q. Li, C.E. Snape, Comparison of the impact of moisture on methane adsorption and nanoporosity for over mature shales and their kerogens, Int. J. Coal Geol. 103705 (2021).
- [5] M. Gasparik, P. Bertier, Y. Gensterblum, A. Ghanizadeh, B.M. Krooss, R. Littke, Geological controls on the methane storage capacity in organic-rich shales, Int. J. Coal Geol. 123 (2014) 34–51.
- [6] T.F. Rexer, E.J. Mathia, A.C. Aplin, K.M. Thomas, High-pressure methane adsorption and characterization of pores in Posidonia shales and isolated kerogens, Energy Fuels 28 (5) (2014) 2886–2901.
- [7] J. Colléll, G. Galliero, R. Vermorel, P. Ungerer, M. Yiannourakou, F. Montel, M. Pujol, Transport of multicomponent hydrocarbon mixtures in shale organic matter by molecular simulations, J. Phys. Chem. C 119 (39) (2015) 22587–22595.
- [8] E. Fan, S. Tang, C. Zhang, Q. Guo, C. Sun, Methane sorption capacity of organics and clays in high-over matured shale-gas systems, Energy Explor. Exploit. 32 (6) (2014) 927–942.
- [9] D.V. Krevelen, Coal: typology, chemistry, physics, Constitution 3 (1961).
- [10] B. Tissot, Recent advances in petroleum geochemistry applied to hydrocarbon exploration, AAPG Bull. 68 (5) (1984) 545–563.
- [11] W.G. Dow, Kerogen studies and geological interpretations, J. Geochem. Explor. 7 (1977) 79–99.
- [12] B. Durand, Kerogen: Insoluble organic matter from sedimentary rocks, Editions technip1980.
- [13] F. Behar, M. Vandenbroucke, Chemical modelling of kerogens, Org Geochem. 11 (1) (1987) 15–24.
- [14] W. Li, L.A. Stevens, W. Meredith, C.N. Uguna, C.H. Vane, B. Zhang, A.D. Carr, D. Zheng, C.E. Snape, The effect of oil extraction on porosity and methane adsorption for dry and moisture-equilibrated shales, Fuel 316 (2022), 123304.
- [15] P. Whitelaw, C.N. Uguna, L.A. Stevens, W. Meredith, C.E. Snape, C.H. Vane, V. Moss-Hayes, A.D. Carr, Shale gas reserve evaluation by laboratory pyrolysis and gas holding capacity consistent with field data, Nat. Commun. 10 (1) (2019) 1–10.
- [16] W. Li, X. Pang, C. Snape, B. Zhang, D. Zheng, X. Zhang, Molecular simulation study on methane adsorption capacity and mechanism in clay minerals: effect of clay type, Pressure, and Water Saturation in Shales, Energy & Fuels 33 (2) (2019) 765–778.

- [17] A. Merkel, R. Fink, R. Littke, High pressure methane sorption characteristics of lacustrine shales from the Midland Valley Basin, Scotland, *Fuel* 182 (2016) 361–372.
- [18] M. Wang, D. Zhang, Influences of moisture on adsorption and desorption of methane on gas shales, *Energy Sources Part A* (2020) 1–19.
- [19] J. Li, X. Li, X. Wang, Y. Li, K. Wu, J. Shi, L. Yang, D. Feng, T. Zhang, P. Yu, Water distribution characteristic and effect on methane adsorption capacity in shale clay, *Int. J. Coal Geol.* 159 (2016) 135–154.
- [20] J. Zou, R. Rezaee, Q. Xie, L. You, K. Liu, A. Saeedi, Investigation of moisture effect on methane adsorption capacity of shale samples, *Fuel* 232 (2018) 323–332.
- [21] R. Heller, M. Zoback, Adsorption of methane and carbon dioxide on gas shale and pure mineral samples, *Journal of Unconventional Oil and Gas, Resources* 8 (2014) 14–24.
- [22] A. Zolfaghari, H. Dehghanpour, J. Holyk, Water sorption behaviour of gas shales: I. Role of clays, *Int. J. Coal Geol.* 179 (2017) 130–138.
- [23] X. Tang, N. Ripepi, K.A. Valentine, C. Keles, T. Long, A. Gonciaruk, Water vapor sorption on Marcellus shale: measurement, modeling and thermodynamic analysis, *Fuel* 209 (2017) 606–614.
- [24] P. Luo, N. Zhong, I. Khan, X. Wang, H. Wang, Q. Luo, Z. Guo, Effects of pore structure and wettability on methane adsorption capacity of mud rock: Insights from mixture of organic matter and clay minerals, *Fuel* 251 (2019) 551–561.
- [25] G. Sang, S. Liu, D. Elsworth, Water vapor sorption properties of Illinois shales under dynamic water vapor conditions: experimentation and modeling, *Water Resour. Res.* 55 (8) (2019) 7212–7228.
- [26] J. Bai, Y. Kang, M. Chen, Z. Chen, L. You, X. Li, G. Chen, Impact of surface chemistry and pore structure on water vapor adsorption behavior in gas shale, *Chem. Eng. J.* 402 (2020), 126238.
- [27] Y. Yang, J. Liu, J. Yao, J. Kou, Z. Li, T. Wu, K. Zhang, L. Zhang, H. Sun, Adsorption behaviors of shale oil in kerogen slit by molecular simulation, *Chem. Eng. J.* 387 (2020), 124054.
- [28] J. Cao, Y. Liang, Y. Masuda, H. Koga, H. Tanaka, K. Tamura, S. Takagi, T. Matsuoka, Molecular Simulation of Methane Adsorption Behavior in Kerogen Nanopores for Shale Gas Resource Assessment, International Petroleum Technology Conference, International Petroleum Technology Conference, 2019.
- [29] J. Collett, P. Ungerer, G. Galliero, M. Yiannourakou, F.O., Montel, M., Pujol, Molecular simulation of bulk organic matter in type II shales in the middle of the oil formation window, *Energy Fuels* 28 (12) (2014) 7457–7466.
- [30] L. Huang, Z. Ning, Q. Wang, W. Zhang, Z. Cheng, X. Wu, H. Qin, Effect of organic type and moisture on CO<sub>2</sub>/CH<sub>4</sub> competitive adsorption in kerogen with implications for CO<sub>2</sub> sequestration and enhanced CH<sub>4</sub> recovery, *Appl. Energy* 210 (2018) 28–43.
- [31] R. Wang, J. Li, L. Gibellia, Z. Guo, M.K. Borg, Sub-nanometre pore adsorption of methane in kerogen, *Chem. Eng. J.* 130984 (2021).
- [32] R. Sadus, *Molecular Simulation Of Fluids*, Elsevier, 2002.
- [33] D. Frenkel, B. Smit, *Understanding Molecular Simulation: From Algorithms To Applications*, Elsevier, 2001.
- [34] L. Wang, J. Liu, W. Song, H. Wang, Y. Li, J. Liu, Z. Zhao, J. Tan, Z. Duan, J. Deng, Experimental and DFT insights of BiVO<sub>4</sub> as an effective photocatalytic catalyst for N<sub>2</sub>O decomposition, *Chem. Eng. J.* 366 (2019) 504–513.
- [35] B. Tissot, WELTED, H.(1984) *Petroleum Formation and Occurrence*, Berlin (Springer-Verlag) (1984).
- [36] M. Djuricic, R. Murphy, D. Vitorovic, K. Biemann, Organic acids obtained by alkaline permanganate oxidation of kerogen from the Green River (Colorado) shale, *Geochim. Cosmochim. Acta* 35 (12) (1971) 1201–1207.
- [37] S. Kelemen, M. Afeworki, M. Gorbati, M. Sansone, P. Kwiatak, C. Walters, H. Freund, M. Siskin, A. Bence, D. Curry, Direct characterization of kerogen by X-ray and solid-state <sup>13</sup>C nuclear magnetic resonance methods, *Energy Fuels* 21 (3) (2007) 1548–1561.
- [38] P. Ungerer, J. Collett, M. Yiannourakou, Molecular modeling of the volumetric and thermodynamic properties of kerogen: Influence of organic type and maturity, *Energy Fuels* 29 (1) (2015) 91–105.
- [39] W. Li, L.A. Stevens, B. Zhang, D. Zheng, C.E. Snape, Combining molecular simulation and experiment to prove micropore distribution controls methane adsorption in kerogens, *Int. J. Coal Geol.* 104092 (2022).
- [40] S.p., Tesson, A., Firoozabadi, Methane adsorption and self-diffusion in shale kerogen and slit nanopores by molecular simulations, *The Journal of Physical Chemistry C* 122 (41) (2018) 23528–23542.
- [41] L. Michalec, M. Lisal, Molecular simulation of shale gas adsorption onto overmature type II model kerogen with control microporosity, *Mol. Phys.* 115 (9–12) (2017) 1086–1103.
- [42] S. Wang, X. Yao, Q. Feng, F. Javadpour, Y. Yang, Q. Xue, X. Li, Molecular insights into carbon dioxide enhanced multi-component shale gas recovery and its sequestration in realistic kerogen, *Chem. Eng. J.* 425 (2021), 130292.
- [43] J. Xiong, X. Liu, L. Liang, Q. Zeng, Adsorption of methane in organic-rich shale nanopores: An experimental and molecular simulation study, *Fuel* 200 (2017) 299–315.
- [44] M. Firouzi, E.C. Rupp, C.W. Liu, J. Wilcox, Molecular simulation and experimental characterization of the nanoporous structures of coal and gas shale, *Int. J. Coal Geol.* 121 (2014) 123–128.
- [45] L. Huang, Z. Ning, Q. Wang, R. Qi, Z. Cheng, X. Wu, W. Zhang, H. Qin, Molecular insights into kerogen deformation induced by CO<sub>2</sub>/CH<sub>4</sub> sorption: effect of maturity and moisture, *Energy Fuels* 33 (6) (2019) 4792–4805.
- [46] L. Chong, S. Sanguinito, A.L. Goodman, E.M. Myshakin, Molecular characterization of carbon dioxide, methane, and water adsorption in micropore space of kerogen matrix, *Fuel* 283 (2021), 119254.
- [47] F. Guo, S. Wang, Q. Feng, X. Yao, Q. Xue, X. Li, Adsorption and absorption of supercritical methane within shale kerogen slit, *J. Mol. Liq.* 320 (2020), 114364.
- [48] J. Liu, Y. Yang, S. Sun, J. Yao, J. Kou, Flow Behaviors of Shale Oil in Kerogen Slit by Molecular Dynamics Simulation, *Chem. Eng. J.* 134682 (2022).
- [49] W. Zhou, H. Wang, X. Yang, X. Liu, Y. Yan, Confinement effects and CO<sub>2</sub>/CH<sub>4</sub> competitive adsorption in realistic shale kerogen nanopores, *Ind. Eng. Chem. Res.* 59 (14) (2020) 6696–6706.
- [50] S. Wang, Y. Liang, Q. Feng, F. Javadpour, Sticky layers affect oil transport through the nanopores of realistic shale kerogen, *Fuel* 310 (2022), 122480.
- [51] Z. Sun, X. Li, W. Liu, T. Zhang, M. He, H. Nasrabadi, Molecular dynamics of methane flow behavior through realistic organic nanopores under geologic shale condition: pore size and kerogen types, *Chem. Eng. J.* 398 (2020), 124341.
- [52] J. Zhou, Q. Mao, K.H. Luo, Effects of moisture and salinity on methane adsorption in kerogen: a molecular simulation study, *Energy Fuels* 33 (6) (2019) 5368–5376.
- [53] L. Huang, Z. Ning, Q. Wang, R. Qi, Y. Zeng, H. Qin, H. Ye, W. Zhang, Molecular simulation of adsorption behaviors of methane, carbon dioxide and their mixtures on kerogen: effect of kerogen maturity and moisture content, *Fuel* 211 (2018) 159–172.
- [54] T. Zhao, X. Li, H. Zhao, M. Li, Molecular simulation of adsorption and thermodynamic properties on type II kerogen: Influence of maturity and moisture content, *Fuel* 190 (2017) 198–207.
- [55] L. Gong, J.-H. Shi, B. Ding, Z.-Q. Huang, S.-Y. Sun, J. Yao, Molecular insight on competitive adsorption and diffusion characteristics of shale gas in water-bearing channels, *Fuel* 278 (2020), 118406.
- [56] T. Zhao, X. Li, Z. Ning, H. Zhao, M. Li, Molecular simulation of methane adsorption on type II kerogen with the impact of water content, *J. Petrol. Sci. Eng.* 161 (2018) 302–310.
- [57] J. Zhang, M. Clennell, D. Dewhurst, K. Liu, Combined Monte Carlo and molecular dynamics simulation of methane adsorption on dry and moist coal, *Fuel* 122 (2014) 186–197.
- [58] R. Fry, S. Day, R. Sakurovs, Moisture-induced swelling of coal, *Internat. J. Coal Prep. Utiliz.* 29 (6) (2009) 298–316.
- [59] M. Gasparik, A. Ghanizadeh, Y. Gensterblum, B.M. Krooss, “Multi-temperature” method for high-pressure sorption measurements on moist shales, *Rev. Sci. Instrum.* 84 (8) (2013), 085116.
- [60] M. Thommes, K. Kaneko, A.V. Neimark, J.P. Olivier, F. Rodriguez-Reinoso, J. Rouquerol, K.S. Sing, Physisorption of gases, with special reference to the evaluation of surface area and pore size distribution (IUPAC Technical Report), *Pure Appl. Chem.* 87 (9–10) (2015) 1051–1069.
- [61] C. Zou, D. Dong, S. Wang, J. Li, X. Li, Y. Wang, D. Li, K. Cheng, Geological characteristics and resource potential of shale gas in China, *Pet. Explor. Dev.* 37 (6) (2010) 641–653.
- [62] I.J. Andrews, *The Carboniferous Bowland Shale gas study: geology and resource estimation*, (2013).
- [63] H. Clarke, P. Turner, R.M. Bustin, N. Riley, B. Besly, Shale gas resources of the Bowland Basin, NW England: a holistic study, *Petrol. Geosci.* 24 (3) (2018) 287–322.
- [64] J.F. Young, Humidity control in the laboratory using salt solutions—a review, *J. Appl. Chem.* 17 (9) (1967) 241–245.
- [65] H. Sun, COMPASS: an ab initio force-field optimized for condensed-phase applications overview with details on alkane and benzene compounds, *J. Phys. Chem. B* 102 (38) (1998) 7338–7364.
- [66] H. Sui, J. Yao, Effect of surface chemistry for CH<sub>4</sub>/CO<sub>2</sub> adsorption in kerogen: A molecular simulation study, *J. Nat. Gas Sci. Eng.* 31 (2016) 738–746.
- [67] S.p., Tesson, A., Firoozabadi, Deformation and swelling of kerogen matrix in light hydrocarbons and carbon dioxide, *J. Phys. Chem. C* 123 (48) (2019) 29173–29183.
- [68] S. Nosé, A unified formulation of the constant temperature molecular dynamics methods, *J. Chem. Phys.* 81 (1) (1984) 511–519.
- [69] S. Nosé, A molecular dynamics method for simulations in the canonical ensemble, *Mol. Phys.* 52 (2) (1984) 255–268.
- [70] S. Nosé, M.L. Klein, A study of solid and liquid carbon tetrafluoride using the constant pressure molecular dynamics technique, *J. Chem. Phys.* 78 (11) (1983) 6928–6939.
- [71] W.G. Hoover, Constant-pressure equations of motion, *Phys. Rev. A* 34 (3) (1986) 2499.
- [72] Z. Wang, W. Su, X. Tang, J. Wu, Influence of water invasion on methane adsorption behavior in coal, *Int. J. Coal Geol.* 197 (2018) 74–83.
- [73] F. Van Bergen, C. Spiers, G. Floor, P. Bots, Strain development in unconfined coals exposed to CO<sub>2</sub>, CH<sub>4</sub> and Ar: effect of moisture, *Int. J. Coal Geol.* 77 (1–2) (2009) 43–53.
- [74] P.M. Mathias, T.W. Copeman, Extension of the Peng-Robinson equation of state to complex mixtures: evaluation of the various forms of the local composition concept, *Fluid Phase Equilib.* 13 (1983) 91–108.
- [75] M.L. Connolly, Solvent-accessible surfaces of proteins and nucleic acids, *Science* 221 (4612) (1983) 709–713.
- [76] G. Aguilar-Armenta, M.E. Patiño-Iglesias, R. Leyva-Ramos, Adsorption kinetic behaviour of pure CO<sub>2</sub>, N<sub>2</sub> and CH<sub>4</sub> in natural clinoptilolite at different temperatures, *Adsorpt. Sci. Technol.* 21 (1) (2003) 81–91.
- [77] A.F. Ismail, K.C. Khulbe, T. Matsuura, Gas separation membranes, *Switz. Springer* 10 (2015) 978–1973.
- [78] C. Largeau, S. Derenne, E. Casadevall, C. Berkalo, M. Corolleur, B. Lugardon, J. Raynaud, J. Connan, Occurrence and origin of “ultralaminar” structures in “amorphous” kerogens of various source rocks and oil shales, *Org. Geochem.* 16 (4–6) (1990) 889–895.



- [79] A. Jagadisan, A. Yang, Z. Heidari, Experimental quantification of the impact of thermal maturity on kerogen density, *Petrophysics-The SPWLA J. Form. Eval. Reserv. Descript.* 58 (06) (2017) 603–612.
- [80] A. Gonciaruk, M.R. Hall, M.W. Fay, C.D. Parmenter, C.H. Vane, A.N. Khlobystov, N. Ripepi, Kerogen nanoscale structure and CO<sub>2</sub> adsorption in shale micropores, *Sci. Rep.* 11 (1) (2021) 1–13.
- [81] C.a. Wang, T. Huddle, C.-H. Huang, W. Zhu, R.L. Vander Wal, E.H. Lester, J.P. Mathews, Improved quantification of curvature in high-resolution transmission electron microscopy lattice fringe micrographs of soots, *Carbon* 117 (2017) 174–181.
- [82] K.S. Okiongbo, A.C. Aplin, S.R. Larter, Changes in type II kerogen density as a function of maturity: Evidence from the Kimmeridge Clay Formation, *Energy Fuels* 19 (6) (2005) 2495–2499.
- [83] A. Stankiewicz\*, B. Bennett, O. Wint, N. Ionkina, B. Motherwell, M. Mastalerz, Kerogen density revisited—lessons from the Duvernay Shale, *Unconventional Resources Technology Conference*, San Antonio, Texas, 20–22 July 2015, Society of Exploration Geophysicists, American Association of Petroleum ..., 2015, pp. 864–874.
- [84] W.A. Hartgers, J.S.S. Damsté, J.W. De Leeuw, Y. Ling, J.C. Crelling, The influence of mineral matter on the separation of amorphous marine kerogens using density gradient centrifugation, *Org. Geochem.* 23 (8) (1995) 777–784.
- [85] M. Vandenbroucke, C. Largeau, Kerogen origin, evolution and structure, *Org. Geochem.* 38 (5) (2007) 719–833.
- [86] F. Perez, D. Devegoda, Estimation of adsorbed-phase density of methane in realistic overmature kerogen models using molecular simulations for accurate gas in place calculations, *J. Nat. Gas Sci. Eng.* 46 (2017) 865–872.
- [87] K. Fan, Y. Li, D. Elsworth, M. Dong, C. Yin, Y. Li, Z. Chen, Three stages of methane adsorption capacity affected by moisture content, *Fuel* 231 (2018) 352–360.
- [88] L. Fisher, J. Israelachvili, Direct experimental verification of the Kelvin equation for capillary condensation, *Nature* 277 (5697) (1979) 548–549.
- [89] M. Polanyi, The potential theory of adsorption, *Science* 141 (3585) (1963) 1010–1013.
- [90] S. Kumar, M. Prasad, R. Pini, Selective adsorptives to study pore structure and wetting behavior of self-resourcing shales, *SPWLA 56th Annual Logging Symposium*, OnePetro, 2015.
- [91] B.V. Krooss, F. Van Bergen, Y. Gensterblum, N. Siemons, H. Pagnier, P. David, High-pressure methane and carbon dioxide adsorption on dry and moisture-equilibrated Pennsylvanian coals, *Int. J. Coal Geol.* 51 (2) (2002) 69–92.
- [92] G.R. Chalmers, R.M. Bustin, The organic matter distribution and methane capacity of the Lower Cretaceous strata of Northeastern British Columbia, Canada, *Internat. J. Coal Geol.* 70 (1–3) (2007) 223–239.